JGR Solid Earth

RESEARCH ARTICLE
10.1029/2023JB027086

Revisiting the San Andreas Heat Flow Paradox From the Perspective of Seismic Efficiency and Elastic Power in Southern California

Malte J. Ziebarth[1,2], John G. Anderson[3], Sebastian von Specht[4,5], Oliver Heidbach[1], and Fabrice Cotton[1,2]

[1]GFZ German Research Centre for Geosciences, Potsdam, Germany, [2]Institute for Geosciences, University of Potsdam, Potsdam, Germany, [3]Nevada Seismological Laboratory, University of Nevada, Reno, NV, USA, [4]Earthquake-Disaster & Risk Evaluation and Management Center (E-DREaM), National Central University, Taoyuan City, Taiwan, [5]Now at University of Potsdam, Institute of Mathematics, Potsdam, Germany

Key Points:

- Heat flow around the San Andreas fault is incompatible with radiated power and elastic input power under simple assumptions
- Regionally, a stochastic view on heat flow and/or an overestimated total elastic power can resolve the paradox
- Locally, a high seismic efficiency or a low scaled energy (radiated energy/seismicmoment) on the San Andreas fault can resolve the paradox

Supporting Information:

Supporting Information may be found in the online version of this article.

Correspondence to:

M. J. Ziebarth,
ziebarth@gfz-potsdam.de

Citation:

Ziebarth, M. J., Anderson, J. G., von Specht, S., Heidbach, O., & Cotton, F. (2023). Revisiting the San Andreas heat flow paradox from the perspective of seismic efficiency and elastic power in Southern California. *Journal of Geophysical Research: Solid Earth*, *128*, e2023JB027086. https://doi.org/10.1029/2023JB027086

Received 12 MAY 2023
Accepted 20 NOV 2023

Author Contributions:

Conceptualization: Malte J. Ziebarth, John G. Anderson, Sebastian von Specht
Data curation: Malte J. Ziebarth, Sebastian von Specht
Formal analysis: Malte J. Ziebarth, Sebastian von Specht
Funding acquisition: Oliver Heidbach, Fabrice Cotton
Methodology: Malte J. Ziebarth, Sebastian von Specht
Resources: Oliver Heidbach, Fabrice Cotton
Software: Malte J. Ziebarth, John G. Anderson, Sebastian von Specht

Abstract We investigate the relation between frictional heating on a fault and the resulting conductive surface heat flow anomaly using the fault's long-term energy budget. Analysis of the surface heat flow surrounding the fault trace leads to a constraint on the frictional power generated on the fault—the mechanism behind the San Andreas fault (SAF) heat flow paradox. We revisit this paradox from a new perspective using an estimate of the long-term accumulating elastic power in the region surrounding the fault, and analyze the paradox using two parameters: the seismic efficiency and the elastic power. The results show that the constraint on frictional power from the classic interpretation is incompatible with the accumulating elastic power and the radiated power from earthquake catalogs. We then explore four mechanisms that can resolve this extended paradox. First, stochastic fluctuations of surface heat flow could mask the fault-generated anomaly (we estimate 21% probability). Second, the elastic power accumulating in the region could be overestimated (≥550 MW required). Third, the seismic efficiency—ratio of radiated energy to elastic work—of the SAF could be higher than that of the remaining faults in the region (≥5.8% required). Fourth, the scaled energy—ratio of radiated energy to seismic moment—on the SAF could be lower than on the remaining faults in the region (a factor 5 difference required). In the last three hypotheses, we analyze the interplay of the energy budget on a single fault with the total energy budget of the region.

Plain Language Summary When earthquakes move rock against rock, friction heats the contact surface. If this frictional resistance were like laboratory measurements of typical crustal rock, the heat would cause a considerable heat flow signature ("anomaly") at Earth's surface. For the San Andreas fault (SAF) in Southern California, such a signature has not been observed. One solution to this paradox is that the fault is weak. We approach the paradox from a new angle by using additionally the rate at which elastic energy accumulates in California. This elastic power is incompatible with the radiated power from earthquake catalogs and the maximum rate of frictional heating from the paradox if only simple assumptions are made. We call this conflict the extended heat flow paradox. Four mechanisms could individually resolve the extended paradox: randomness in regional heat flow measurements could conceal the anomaly, the elastic power on the SAF could be overestimated, the seismic efficiency (ratio of radiated energy per input work) on the SAF could be comparatively high, or the scaled energy (ratio of radiated energy per seismic moment) on the SAF could be comparatively low. A combination of multiple effects is possible.

1. Introduction

Earthquakes and the related shaking are directly linked to the radiated energy. This energy has to be available on the causative fault before the earthquake. Therefore, the quantification of seismic hazard can also benefit from an understanding of the long-term energy budget of active faults (e.g., Ziebarth et al., 2020). We define the energy budget through the rate at which energy available to cause earthquakes increases between earthquakes. Over the long term, we expect that this increase in potential earthquake energy will be balanced by the energy that is released in earthquakes. For each individual earthquake, the released energy is divided into three constituent parts: radiated energy, frictional heat energy on the fault (Dahlen, 1977), and surface energy required for breaking intact rocks (Lachenbruch & Sass, 1980). Considering the fundamental role of conservation of energy in every

Supervision: Oliver Heidbach, Fabrice Cotton
Validation: John G. Anderson
Visualization: Malte J. Ziebarth
Writing – original draft: Malte J. Ziebarth
Writing – review & editing: Malte J. Ziebarth, John G. Anderson, Sebastian von Specht, Oliver Heidbach, Fabrice Cotton

field of physics, we expect that knowledge of the seismic energy budget is important for understanding the physics of the seismic source and for seismic hazard applications.

What has been missing in previous studies of the earthquake process is an effort to estimate the rate at which potential earthquake energy increases, that is, the input power. Recently, Ziebarth et al. (2020) proposed a method to estimate the input power. They assume a long-term stationary seismicity, translate the energy balance of individual earthquakes to a balance of power, and name the resulting framework the "Energy-Conserving Seismicity" (ENCOS) framework. Their estimate of the input power combines the strain rate tensor, frequently used in seismicity modeling (e.g., J. G. Anderson, 1979; Bird et al., 2010; Molnar, 1979), with the stress tensor. The input power is consistent with the rate of large earthquakes in Southern California.

While the variables in the energy budget are known, it is not easy to quantify the fraction of energy that is released into each constituent part in large earthquakes. The radiated energy is determined best as it can be estimated using the energy that is carried in the observed seismic waves. A key parameter is the seismic efficiency, which is the fraction of the total released energy that goes into the radiated energy. The causative fault is not observable, so the heat energy and surface energy must be inferred. It is generally believed that the largest earthquakes occur on well-developed faults, so the surface energy is generally assumed to be negligible. A potential constraint on heat generation are heat flow measurements on the surface above the fault (e.g., Brune et al., 1969; Henyey & Wasserburg, 1971; Lachenbruch & Sass, 1980). Thus, a location where the input energy can be estimated, the rate of the largest earthquakes is approximately known, and heat flow measurements are available provides conditions in which the parameters of the ENCOS model can possibly be constrained. This, in turn, could help to constrain the long-term rate of radiated energy, and thereby shaking, of large earthquakes.

For the San Andreas fault (SAF) in California, the fault's contribution to surface heat flow has been observed to be low, resulting in the conclusion that friction on the fault is also low (Brune et al., 1969; Lachenbruch & Sass, 1980). This conclusion runs into difficulty when the typical friction ($\mu \geq 0.6$) between rocks is considered (Byerlee, 1978; Scholz, 2006). This inconsistency is termed the "heat [flow] paradox" (Lachenbruch & Sass, 1988; Lambert et al., 2021). Given the input power based on the ENCOS framework and an estimate of the rate of earthquakes, the seismic efficiency and frictional power must trade off. A close look at the heat flow paradox becomes justified in this context.

In this paper, we define a two-dimensional parameter space using the input power and the seismic efficiency. We then use the rates of earthquakes and the observed heat flow to rigorously determine the allowed ranges of these parameters. This expands the space in which the heat flow paradox is analyzed. Through this, we impose a new constraint on the overall earthquake energy budget. We test our new approach at the SAF where the heat flow paradox has been examined in detail and additional input data sets are available. Furthermore, our approach improves our understanding of the regional deformation and seismic energy partitioning, and provides an avenue to employ energy to constrain seismic hazard estimates.

2. Theory

2.1. Workflow Synopsis

To connect the classical heat flow paradox with the long-term seismic energy budget we follow three conceptual steps as illustrated in Figure 1. These three steps are described in the following and formally derived in the theory Section 2.3.

1. The interseismic tectonic strain accumulates energy at a constant rate $\dot{E}$ which is released (averaged over many earthquakes) mostly as radiated power P_r and frictional dissipation P_H on a fault. At long time scales, the averaged P_H produces a conductive heat flow anomaly on Earth's surface above the fault following Lachenbruch and Sass (1980) (panel 1).
2. The heat flow anomaly is a function of frictional power P_H. If P_H were chosen to be too large, the anomaly would conflict with the heat flow measurements by evidently diverging from the spatial pattern of heat flow. Thus, this constrains the assumptions on P_H (panel 2).
3. The frictional dissipation power P_H can be contoured as a function of $\dot{E}$ and long-term average seismic efficiency $\bar{\eta}$. Through the constraint on P_H from the heat flow data, we can constrain the parameter space of $\bar{\eta}$ and $\dot{E}$. If the elastic power is too large and the seismic efficiency is too low, the resulting dissipation P_H would

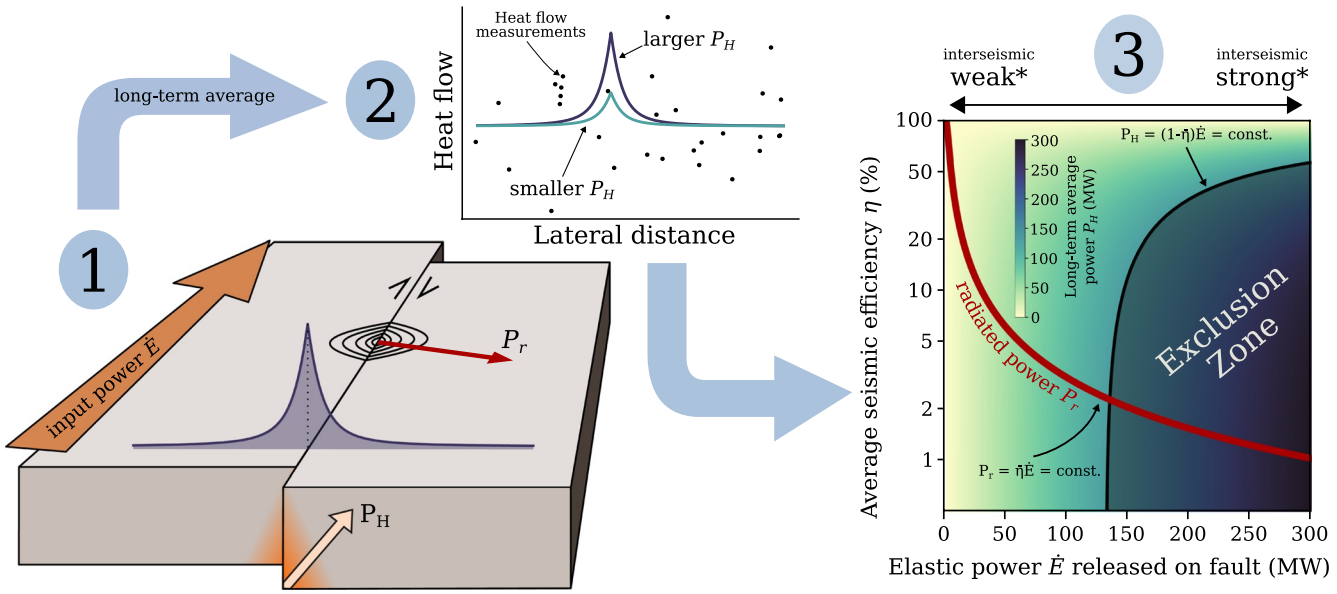

Figure 1. The workflow described in Section 2.1. (1) Interseismic tectonic strain accumulates energy at a rate $\dot{E}$ which is released, averaged over many earthquakes, mostly as radiated power P_r and frictional dissipation P_H on a fault. At long time scales, the averaged dissipation P_H produces a conductive heat flow anomaly on Earth's surface above the fault (pointed graph, here shown for a vertical strike-slip fault following Lachenbruch and Sass (1980)). (2) The heat flow anomaly is a function of frictional power P_H. We aim to answer how strong the anomaly can be before it conflicts with heat flow measurements. Vice versa, the heat flow constrains P_H. (3) P_H is a function of $\dot{E}$ and average seismic efficiency $\bar{\eta}$ as higher $\dot{E}$ or smaller efficiency lead to more heat released on the fault. Thus, through the constraint on P_H from the heat flow data we can constrain the parameter space of the long-term average seismic efficiency $\bar{\eta}$ and elastic loading power $\dot{E}$. A part of that parameter space is excluded. The radiated power P_r can also be evaluated from $\dot{E}$ and $\bar{\eta}$, which—at constant P_r—leads to a downward curve similar to the thick red one. Thus limits from the heat flow paradox on P_H (steps 1 and 2) constrain the seismic efficiency and prohibit arbitrary combinations of $\dot{E}$ and P_r that could be accommodated by a freely varying efficiency. (*) At constant slip rate, low or high elastic power corresponds to an interseismically weak or strong fault that allows higher differential stress to be sustained.

cause a large heat flow anomaly that would be in conflict with the heat flow data. This leads to an excluded region in $\dot{E}$-$\bar{\eta}$-space. The boundary of the excluded region is orthogonal to the constraints obtained from an estimate of the radiated power which leads to the downward curve in panel 3. The radiated power and the heat flow hence contain complementary information.

Furthermore, we make the following two model assumptions. First, we do not consider the impact of fluid flow in the heat transport modeling. For the SAF that we use as an example in chapter 3, there is evidence that fluid flow might not play a significant role in heat transport from the fault (Fulton et al., 2004; Lachenbruch & Sass, 1992; Saffer et al., 2003) although specific modes of transport may be possible (Scholz, 2006). A more thorough analysis or a transfer of the workflow to other faults might consider the impact of fluid flow within credible bounds. This impact is controlled mostly by the knowledge of permeability (Fulton et al., 2004), which in turn might be quite uncertain. Similar considerations hold for inhomogeneous thermal conductivity although the effect might generally be less pronounced.

We further assume that the contribution of surface energy required to form the damage zone is negligible when compared against the long-term power budget. For the SAF there are indications that this is a reasonable first-order approximation. Lachenbruch and Sass (1980), for instance, estimate that with a damage zone width of up to 1 km and a total slip of more than 100 km on the SAF the contribution to the energy budget would be negligible to first order.

Another potential energy sink we discard is chemical energy sunk in endothermic reactions that might occur during metamorphism in rocks in the fault damage zone due to the coseismic pressure-temperature conditions (Hamada et al., 2009; Lachenbruch & Sass, 1980). Such a chemical energy sink absorbs some frictional heat directly on the fault surface, reducing the amount of heat that would be transported to generate a surface heat flow anomaly. If the chemical energy sink were significant, this could resolve the heat flow paradox—and would make itself known through the endothermically generated minerals in the fault rock. Although these sinks have been theorized to be significant in favorable mineral composition of the fault rock (Hamada et al., 2009), known

estimates of the chemical energy for the 1999 Chi-Chi earthquake (0.79% of E_H; Hamada et al., 2009) and typical expectation (e.g., Lachenbruch & Sass, 1980; Yang et al., 2020) place the endothermic chemical energy contribution to the fault energy budget at an insignificant level compared to the frictional energy. We hence discard the chemical energy and leave a quantitative estimate for the SAF up for future work.

Following the workflow explained above and the model assumptions we develop in the following three sections the formal framework for our approach.

2.2. Earthquake Energy Budget

When a fault slips, the total amount of strain energy released, ΔE, is converted into multiple other forms of energy (which one might call the energy sinks). A common way to write this conversion is to partition ΔE among fracture energy, E_G, heat dissipation on the fault, E_H^*, and energy radiated away from the fault, E_r (Dahlen, 1977; Husseini, 1977; Orowan, 1949):

$$\Delta E = E_r + E_H^* + E_G. \tag{1}$$

From the four energies of Equation 1, the radiated energy E_r travels off to structurally relevant sites and ultimately determines the seismic hazard. The other two energy sinks, E_H^* and E_G, are products of the physics of fault slip and prerequisites for estimating how much strain energy gets converted into radiated energy. We aim to shed light on these energy sinks by use of the San Andreas heat flow paradox.

To connect the energy partitioning with the heat flow paradox, we need to identify in the right hand side of Equation 2 all energy that eventually becomes heat on or in immediate vicinity of the fault (for brevity we will write "on" henceforth). This energy ultimately drives the surface heat flow anomaly. Although Equation 2 contains the heat term E_H, it is not a directly suitable partitioning for a connection with the heat flow paradox. The reason is that the fracture energy is conventionally defined through dynamic models of rupture (e.g., Cocco et al., 2023; Nielsen et al., 2016), where it describes energy converted in the slip weakening process as opposed to frictional resistance during stable sliding. However, ultimately most of this fracture energy will share the same fate as E_H: heat on the fault (Lachenbruch & Sass, 1980).

Therefore, we use a different energy partitioning, based on microscopic energy types, that is better suited for the heat flow problem:

$$\Delta E = E_r + E_H + E_S + \underbrace{E_C}_{=0} \tag{2}$$

Here E_H is all energy that ends up as heat transmitted from the fault, E_S is the surface energy required to create new fracture (e.g., Lachenbruch & Sass, 1980; Nielsen et al., 2016), and E_C is heat consumed in endothermic metamorphic processes ("chemical energy" which we immediately discard as outlined in Section 2.1). With respect to Equation 1, the fracture energy E_G is split into surface energy and heat ($E_G = E_S + E_{HG}$) and the total heat is composed of E_H^* and the split-off part of the fracture energy $\left(E_H = E_H^* + E_{HG}\right)$.

The significance of the surface energy E_S within the overall energy budget of earthquakes on a fault can vary on a fault-to-fault basis, and is presumably related to the structural maturity of the fault (a measure of the slip history; Guo et al., 2023). For instance, on one end of the maturity scale Zang et al. (2000) find a surface energy of 29% the total work for the creation of a new fracture in granite samples, which is significant compared to both radiated energy and heat (1.5% and 69% of ΔE, respectively). For a single earthquake, Pittarello et al. (2008) estimate that the surface energy is less than 3% of the heat, that is, insignificant compared to E_H but potentially similar to the radiated energy for efficiencies in the order of a few percent (within the range estimated for some events by McGarr, 1999). On the mature side of the scale, Lachenbruch and Sass (1980) estimate surface energy on the SAF within a range that is insignificant compared to both radiated and heat energy (see SI1.4 in the supplementary material). Hence, on our path forward we will assume $E_S = 0$ on mature faults and consequently $\dot{E}_S = P_S = 0$. On immature faults, we will leave the possible contribution of E_S open.

With the ENCOS framework, Ziebarth et al. (2020) show how on long time scales, iterating over many earthquakes, the cumulative energy ΔE may be computed to constrain the budget of radiated energy. In their balance of power, ΔE is replaced by the elastic power $\dot{E}$, which is both the average ΔE per time over many earthquakes

and the elastic power with which ΔE accumulates in the interseismically deformed crust. For instance in the block model shown in Figure 1, $\dot{E}$ is transferred from the moving plates as shear stress on the fault acts against the movement. Averaging the remaining contributions of the energy balance over time and introducing the average seismic efficiency $\bar{\eta}$, the stationary power balance reads

$$\bar{\eta} = \frac{E_r}{\Delta E} = \frac{P_r}{\dot{E}}, \tag{3}$$

$$(1-\bar{\eta})\dot{E} = \begin{cases} P_S + P_H & : \text{non-mature fault} \\ P_H & : \text{mature fault.} \end{cases} \tag{4}$$

The balance of power connects the energy budget of many earthquakes with the analysis of surface heat flow through the average frictional power P_H. On the fault surface, this average power is an oversimplification since it averages large coseismic powers acting on short timescales over long and quiet interseismic times. However, to describe surface heat flow the average power will be useful due to the long characteristic time scale of heat transfer.

In the following sections, we often shorten "average seismic efficiency" to "seismic efficiency" for brevity and use the bar ($\bar{\eta}$) to distinguish the average seismic efficiency from the single-event seismic efficiency (η).

2.3. Introduction to the Heat Flow Problem

We will now consider the issues related to the fate of the heat generated on the mature fault in more detail. The frictional heat E_H of a single earthquake will be dissipated with high density on and in the immediate vicinity of the fault plane. For instance, in case of the 1999 Chi-Chi earthquake, a significant temperature increase was localized within 30 m of the fault plane 5 years after the event (Kano et al., 2006). For a conductive process, the cumulative heat flow from ruptures on the fault over hundreds of thousands to millions of years can be significant enough to become an additive factor that is superimposed on the background of heat flow from other sources. The challenge is to constrain the strength of this anomaly in the presence of seemingly random fluctuations, noise, in the background heat flow. Our path forward will be to express the expected surface heat flow anomaly in terms of the fault energy budget, and employ a Bayesian method to infer the strength of this anomaly under consideration of the fluctuations and their uncertainties. This section is tailored to the subsequent application to the SAF which will motivate assumptions for mature faults in general ($P_S = 0$) and the SAF in particular.

After being generated on the fault surface, three main modes of heat transfer are available to transport the heat in a brittle crust: conductive heat transfer, and advection either through pore fluids (Hewitt, 2020; Lachenbruch & Sass, 1980) or moving rock mass (Molnar & England, 1990). Pore water-based advection is attributed to either external ground water flow or convection (Gupta, 2011). Following Saffer et al. (2003) and Fulton et al. (2004), we discard fluid-based advection for our application to the San Andreas fault. Advection through rock mass occurs in seismic or aseismic fault movement. For the analysis of fault-generated heat flow, advection through rock mass is particularly relevant in normal and thrust faulting but not in case of strike-slip faulting, where the rock movement is orthogonal to the anomaly (see the geometry sketch in Figure 1). We thus discard rock mass advection as well.

In our purely conductive setting, the heat transport in a temperature field T is governed by the heat equation

$$\frac{\partial T}{\partial t} = \nabla(\kappa \nabla T) = \kappa \nabla^2 T, \tag{5}$$

where the second equality is limited to the case of a homogeneous thermal diffusivity κ.

This equation leads to a characteristic time scale L^2/κ (see e.g., Crank, 1975), the time at which the diffusion front has traveled a distance L. For crystalline rock with diffusivity in the order of $\kappa \approx 1$ mm^2/s (Drury, 1987) and a length scale $L = 1$ km, the characteristic time scale is about 30 ka, large enough to cover a few return periods of large earthquakes on active faults. With most of the heat generated several kilometers below the surface, heat flow observations average over many return periods. This allows us to describe heat production on the fault by a constant power P_H.

The heat transport Equation 5 and P_H are connected by integrating the time-averaged heat flow $\vec{q}$, a boundary condition of Equation 5, over the two sides of the fault surface:

$$P_H = \int_{S^{\pm}} \mathrm{d}\vec{A} \cdot \vec{q}. \tag{6}$$

Lachenbruch and Sass (1980) give an analytical solution for a fault-generated lateral heat flow anomaly in case of a vertical fault from depth d to the surface in a homogeneous medium and heat generation linearly increasing with depth up to a maximum Q^*:

$$q_a(x) = \frac{Q^*}{\pi}\left(1 - \frac{x}{d}\arctan\frac{d}{x}\right) \quad \text{for} \quad t \to \infty. \tag{7}$$

This shape of surface heat flow is shown in the sketch Figure 1. The model leads to a heat production $\bar{Q}d = Q^*d/2$ per unit length of the fault. We can balance this with the total frictional power P_H on a fault segment of length L within a region to relate this anomaly to the $(\dot{E}, \bar{\eta})$ space of the ENCOS long-term seismicity description:

$$\frac{1}{2}Q^*d = \bar{Q}d = \frac{P_H}{L} = \frac{(1-\bar{\eta})\dot{E}}{L}. \tag{8}$$

The last step uses Equation 4 for a mature fault.

Similar to Lachenbruch and Sass, we will apply this model of a fault-generated heat flow anomaly to the SAF in Section 3 and compare the heat flow anomaly to actual heat flow measurements to infer how strong the anomaly can be, but we also introduce the following new ideas:

1. We analyze the strength in terms of the ENCOS parameters $\bar{\eta}$ and $\dot{E}$ instead of the unknown shear stresses on the fault. Through the frictional power P_H connected in Equation 8, a limited anomaly strength Q^* will constrain the parameter space of $\bar{\eta}$ and $\dot{E}$. The constraint, whose shape is shown in step 3 of Figure 1, excludes high-power low-efficiency regions from the plausible parameter combinations (the *exclusion zones*).
2. The long-term radiated power P_r leads to a hyperbolic trade-off between $\dot{E}$ and $\bar{\eta}$ by virtue of Equation 3. An example of how a precisely known P_r can be realized in $(\dot{E}, \bar{\eta})$ space is indicated by the thick downward-trending line in step 3 of Figure 1.
3. We use the model of Ziebarth and von Specht (2023) to estimate to which precision the background heat flow can be assessed and thus estimate the uncertainties in defining the exclusion zones. In other words, exclusion zones can be seen as parts of the parameter space of $\bar{\eta}$ and $\dot{E}$ that are unlikely.

Commonly, the relation of frictional heat to heat flow anomaly is discussed in terms of shear stress or friction coefficient instead of $\bar{\eta}$ and $\dot{E}$. Average frictional shear stress τ_f can be used (e.g., in Lachenbruch & Sass, 1980) to compute $P_H = \tau_f A v$ if the long-term slip rate v of the fault is known. P_H is expressed here through the work $E_H = \tau_f A s$ applied on the fault surface area A over a time Δt. Dividing the slip s by the large time Δt leads to the long-term slip rate v and transforms E_H to P_H. Hence, the use of the frictional power P_H as a description of the heat flow anomaly combines the information from frictional shear stress and long-term fault slip rate into a single variable.

2.4. Quantifying Heat Flow Anomalies

The constraint on P_H through the use of heat flow data requires a decision to be made about whether or not a fault-generated heat flow anomaly is in conflict with the available heat flow measurement data. Previous studies have used a visual comparison of the distinctive fault-lateral graph of the anomaly with the scattered heat flow measurements (e.g., Brune et al., 1969; Fulton et al., 2004; Henyey & Wasserburg, 1971; Lachenbruch & Sass, 1980) as illustrated in Figure 1. This approach has proven very fruitful for the discussion of the heat flow paradox but it has two shortcomings that become important when the decision is used as a basis for further analysis.

First, the visual comparison is foremost a binary classification and subjective expert judgment. Declaring an anomaly of a certain magnitude to be incompatible with the heat flow data directly translates to an upper limit on P_H. If this limit were to be useful, it would have a significant impact on the power balance Equations 3

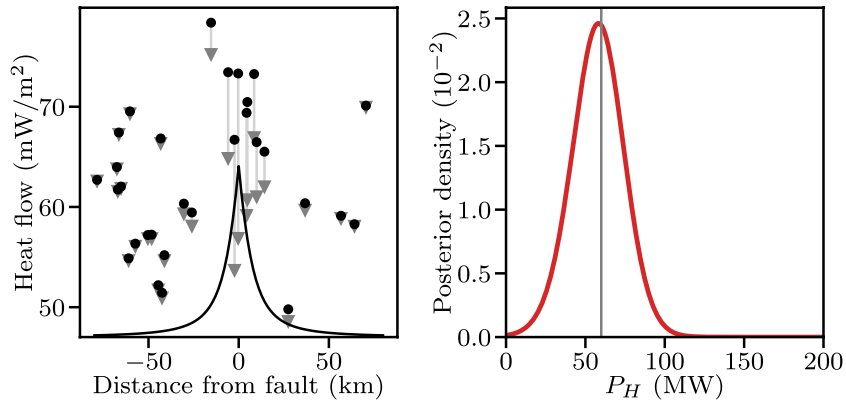

Figure 2. Sketch of the Bayesian analysis of the fault-generated heat flow anomaly strength by Ziebarth and von Specht (2023) using synthetic data. Left: The analysis starts out with heat flow measurements (black dots) in spatial relation to a known strike-slip fault. The heat flow measurements within the investigated region fluctuate as described by Ziebarth and von Specht (2023), and they are distributed according to a probability distribution $p(q)$. These undisturbed fluctuations (gray triangles) are superposed by the fault-generated conductive heat flow anomaly (black line) to yield the measurements. Both the undisturbed data and the anomaly's strength are unknown to the researcher but the anomaly can be modeled as a function of average frictional power P_H. Right: the approach by Ziebarth and von Specht (2023) investigates the continuum of P_H. Each P_H corresponds to a heat flow anomaly of different amplitude, which leads to different corrected data (triangles, left). The likelihood of the corrected data is evaluated against our proposed model of $p(q)$, a gamma distribution, which leads to the posterior of frictional power (thick red line). In case of this synthetic data drawn from a gamma distribution in heat flow and a uniform distribution in distance from the fault, the actual anomaly strength (vertical gray line) is well assessed.

and 4. Then, however, the significant impact on the power balance would be tightly controlled by the expert's decision of the incompatible anomaly magnitude, which hence has to be an unanimous conclusion. To take into account more gradual information, such as considering an anomaly to be unlikely but possible, is complex to formalize to a quantitative scale and might require the judgment of multiple experts (see e.g., Christophersen & Gerstenberger, 2021).

Second, heat flow measurements are inherently noisy on the spatial scale of fault-generated heat flow anomalies (tens of kilometers). This can both be expected from the distribution of radiogenic elements within the crust, which can vary from tens-of-meters to kilometers scale (Jaupart & Mareschal, 2003), and seen from the distribution of heat flow measurements on a global scale, which has a residual variation of about 10–20 mW m^{-2} at a local length scale of 50 km (Goutorbe et al., 2011). This variability causes an inherent uncertainty in the interpretation of the heat flow data and creates a limit for the magnitude of the anomaly that can be excluded: if the anomaly has a smaller magnitude than the fluctuation, it becomes impossible to distinguish it from the noise. This effect might be quite large for the assessment of heat flow anomalies perpendicularly to faults since the number of heat flow data points within the bulk of the anomaly is generally small (often <5–15 in the analysis by Lachenbruch and Sass (1980)). In a visual comparison, the effect of the fluctuations might be quite hard to assess and the quantitative effect of subjective judgment might be enhanced.

For these two reasons, we use the method recently introduced by Ziebarth and von Specht (2023) which we illustrate in Figure 2. The method is based on a reference model, informed by the global heat flow data set of Lucazeau (2019), for the distribution of regional aggregate heat flow, that is, the distribution $p(q)$ of heat flow measurements q_i within a region without considering the spatial distribution. The model, named "REHEATFUNQ" abstracts all kinds of spatial fluctuations of heat flow that can be expected when measuring within in a region of up to 260 km radius. A conductive heat flow anomaly $q_\mathrm{a}(\vec{x})$ can then be identified by comparing the likelihood of the regional heat flow data with that of the data corrected by $q_\mathrm{a}(\vec{x})$. In the Bayesian formulation of Ziebarth and von Specht (2023), this is done via the posterior distribution

$$f(P_H) = \frac{1}{\mathcal{F}} \int_0^\infty \mathrm{d}\alpha \int_0^\infty \mathrm{d}\beta \; p(q_i - q_\mathrm{a}(P_H); \alpha, \beta) \phi(\alpha, \beta) \tag{9}$$

$$q_\mathrm{a}(P_H) = P_H c_i$$

of the frictional power P_H released on the fault. Here, α and β are the parameters of the regional distribution $p(q)$ and $\phi(\alpha, \beta)$ is their prior distribution. We choose the prior parameterization of Ziebarth and von Specht (2023). Finally, c_i quantifies the impact of the fault-generated heat flow anomaly onto data point q_i for a unit frictional power $P_H = 1$. In this article, we compute it by dividing the anomaly Equation 7 at data point x_i by the frictional power P_H.

This method uses the two sources of information available without exact knowledge of the origin of each measurement q_i: the general shape of the regional distribution and the regional data themselves. The Bayesian approach provides a consistent and inter-operable quantification of the uncertainty to which P_H can be inferred. Further information about the origin of the heat flow, for instance from topography or from thermal properties of the crust (Cacace et al., 2013; Fulton et al., 2004), could be included by correcting individual data points.

3. Extending the San Andreas Heat Flow Paradox

With the heat flow paradox connected to the dimensions of long-term elastic power and average seismic efficiency, we now return to the setting that saw the formulation of the original heat flow paradox.

3.1. Study Area & Data

The SAF is a right-lateral continental strike-slip fault, separating the North American plate from the Pacific plate (D. L. Anderson, 1971). Brune et al. (1969) have initiated the discussion about the lack of a heat flow anomaly, and its frictional strength has since been a subject of extensive discussion (e.g., Lachenbruch & Sass, 1980; Scholz, 2006). To model its steady-state heat flow, we hence use the anomaly model Equation 7 following Lachenbruch and Sass (1980). This model choice implies a purely conductive heat transport, which has been supported by the later analysis of Fulton et al. (2004).

We use the SAF geometry from the Uniform California Earthquake Rupture Forecast, version 3 (UCERF3, e.g., Field et al., 2014) fault model 3.2 (Milner, 2014) to locate the data relative to the fault. Figure 3 shows a division of the fault trace from San Bernadino to Point Arena into four regions (a) to (d) that relate to the Mojave, Carrizo, Creeping, and North coast sections of the SAF. This division has also been applied by Ziebarth and von Specht (2023), who found the tightest constraints on the fault-generated heat flow anomaly in the Mojave section. Similarly, Lachenbruch and Sass (1980) found the tightest constraints on the anomaly strength in their region covering the Mojave section, which is roughly contained within region (a) (see Figure 3). Therefore, the focus of our analysis of the SAF-generated heat flow anomaly will be on region (a).

Figure 3 also shows the ROI of Ziebarth et al. (2020), a rectangular region aligned with the SAF and spanning roughly from the Gulf of California to Parkfield. This region is of interest for our study since Ziebarth et al. (2020) have estimated the contemporary rate at which elastic energy accumulates within the crust. In this work, we expand this region ∼10% to the northwest so as to include the epicenter of the 1857 Fort Tejon earthquake, the largest historically recorded earthquake associated with the area. This extended region will be the region representing the "surrounding volume" in our study, comprising of a block representing the crust and, embedded in it, a particular fault for which we can derive energy budget constraints from the heat flow analysis. We will not consider in detail the other faults of the area although many are known in this case.

We use four data sets to derive the extended paradox. First, we use the New Global Heat Flow data set by Lucazeau (2019). Since we use it in combination with the model of Ziebarth and von Specht (2023), we perform the same data filtering: we discard data points of the lowest quality rankings C to F, those earlier than 1990, and negative heat flow values. A side effect is that the data we employ is independent of the data used in the original investigations of the heat flow paradox. Moreover, we remove data points which are not marked as continental crust (key A to H) in field "code1" and those which are categorized as possibly geothermal following Lucazeau (2019) ($q_i > 250$ mW m^{-2}). The remaining data set is shown in Figure 3 (stars).

Furthermore, we use two earthquake catalogs to investigate the radiated energy. We use the historical catalog by Felzer and Cao (2008) for the years 1769–1980, and the catalog by Cheng et al. (2023b) for the years 1981–2021. Figure 4a maps the combined catalog. Finally, we use the UCERF3 model (Milner, 2014) as an alternative means to investigate the radiated energy.

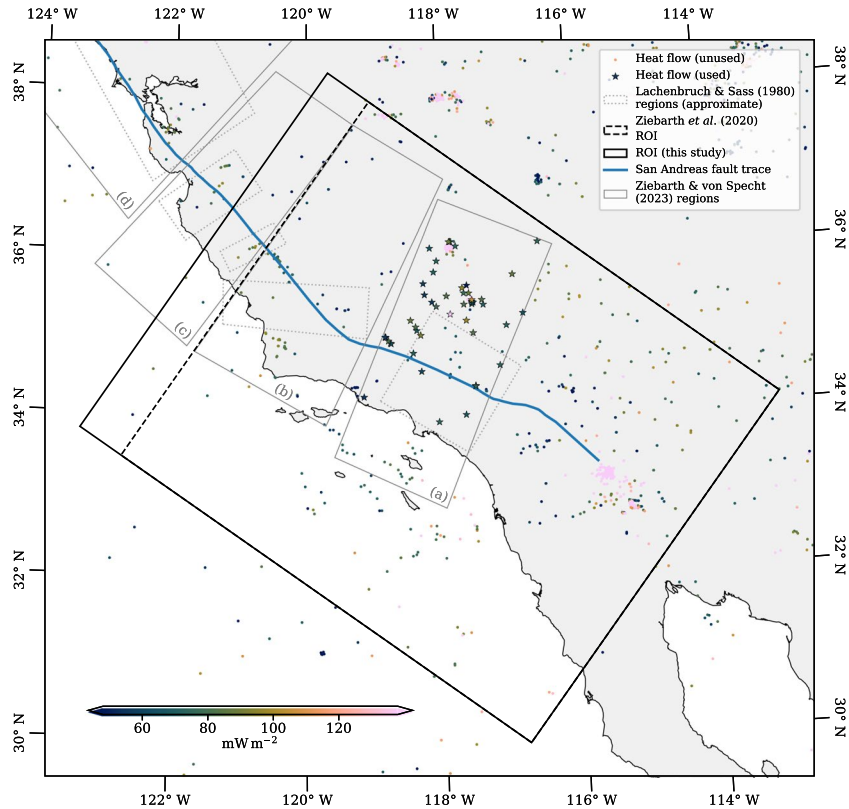

Figure 3. Map of the heat flow data and the different regions of interest (ROI). Dots show the unfiltered data of the NGHF data base within the mapped area (Lucazeau, 2019). Stars show the heat flow data that is used in the analysis by Ziebarth and von Specht (2023) in their region (a) which we use in Section 4.2.1. This data selection has been quality-filtered by criteria due to Lucazeau (2019); Ziebarth and von Specht (2023). The ROI used in this study is derived from the ROI of Ziebarth et al. (2020) by extending it 10% to the north west. The blue San Andreas fault trace stems from the UCERF3 fault model 3.2 (Milner, 2014). The regions of Lachenbruch and Sass (1980) are approximated based on their Figure 8. Shorelines are from the OpenStreetMap database available under the Open Database License.

3.2. The Extended Paradox

We start the analysis by deriving an extended paradox based on a number of observations and model assumptions for the energetics of the San Andreas fault and the surrounding volume. One component of the analysis is the observed seismicity. Using Gutenberg's historical relationship of magnitude and energy,

$$E(M_W) = 10^{1.5M_W+11.8}\,\text{erg} = 10^{1.5M_W+4.8}\,\text{J}, \tag{10}$$

we can compute an average radiated power of an earthquake catalog over its observation period. For the joint catalog (Cheng et al., 2021; Felzer & Cao, 2008), we find

$$P_r = 17\,\text{MW} \tag{11}$$

inside our ROI shown in Figure 4 within the observation period from 1769 to 2021. Using this catalog, we can also estimate the fraction of radiated energy that stems from the SAF. Two of the four largest earthquakes in the catalog, the 1857 M7.9 Fort Tejon earthquake and the 1812 M7.5 Wrightwood earthquake, are associated to the SAF and together accumulate 41% of the cumulative radiated energy of the catalog. Therefore, at least 41% of the radiated energy within the catalog stems from the SAF. We assume that this is representative for the radiated power and make the further assumption that 41% of the elastic power within our ROI is released on the SAF.

We use this ratio in two new variables, ξ and f. Of those, ξ denotes the fraction of radiated power within the ROI that stems from the SAF, and f denotes the fraction of elastic power within the ROI that is released on the SAF:

$$\xi = \frac{P_r^{\text{SAF}}}{P_r}, \tag{12}$$

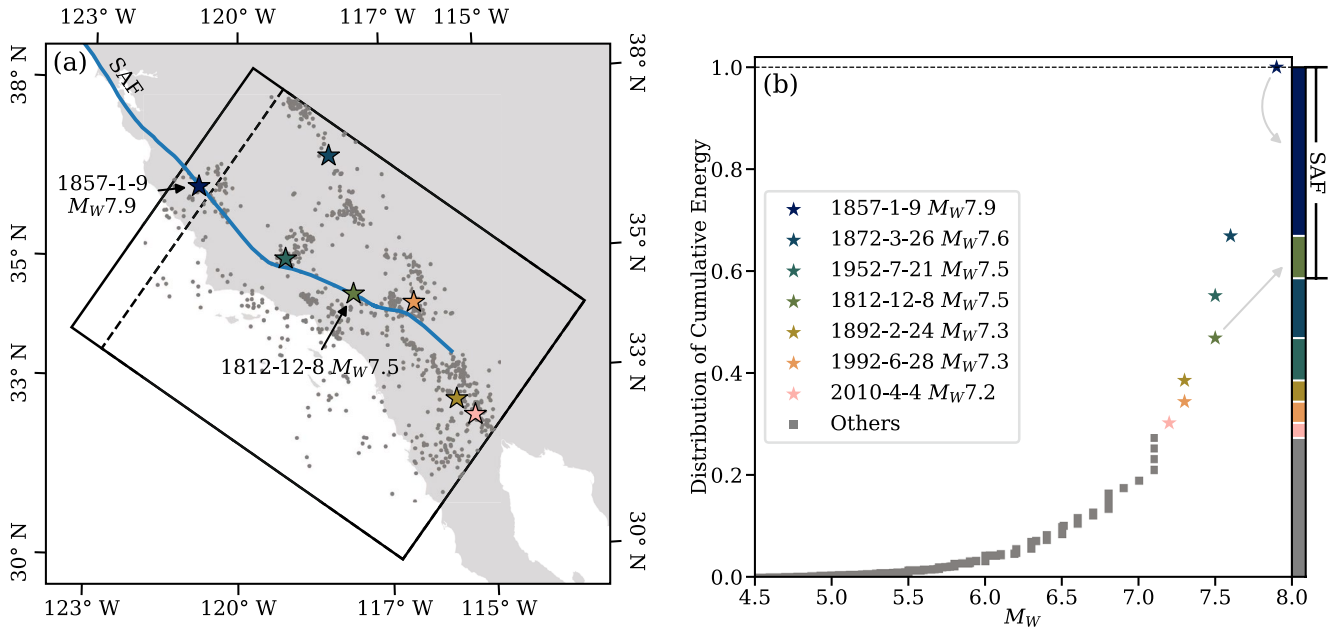

Figure 4. Earthquake catalog and its energies. Panel (a): map of the earthquake catalog. The catalog is a joint catalog comprising the earthquakes of Felzer and Cao (2008) from 1769 to 1980, and the earthquakes of magnitude $M_W \geq 4.5$ of Cheng et al. (2021) from 1981 to 2021. The seven largest earhquakes of the joint catalog are displayed as stars and the remaining 1186 events are plotted anonymously as gray dots. The San Andreas fault trace from the UCERF3 fault model 3.2 is plotted as a thick blue line (Milner, 2014). Two of the seven largest earthquakes, the ones associated to the SAF, are annotated. The rectangular ROI used by Ziebarth et al. (2020) is indicated as a dashed black line and its extension by 10% to the north-west is shown in solid black line. Panel (b): cumulative radiated energy distribution in the joint catalog as a function of earthquake magnitude. Earthquake energy is computed from magnitude using Equation 10. Again, the seven largest earthquakes are marked as stars with colors matching panel (a). The bar plot on the right boundary of the panel shows the cumulative energy distribution reordered so that the two annotated earthquakes of panel (a) are located at the top. Those two earthquakes associated to the SAF account for 50% of the cumulative radiated energy. Shorelines are from the OpenStreetMap database available under the Open Database License.

$$f = \frac{\dot{E}_{\mathrm{SAF}}}{\dot{E}}, \tag{13}$$

$$\xi = f = 41\,\%. \tag{14}$$

With our introductory assumption that the incoming elastic power transforms into radiated and frictional power only, Equation 4, the equality of ξ and f implies that the average seismic efficiency on the SAF is the same as average over the whole ROI. This leads to the following expressions for the radiated and frictional power on the SAF expressed in terms of average seismic efficiency and elastic power of the ROI:

$$P_r^{\mathrm{SAF}} = f\bar{\eta}\dot{E}, \tag{15}$$

$$P_H^{\mathrm{SAF}} = f(1-\bar{\eta})\dot{E}. \tag{16}$$

The elastic power that Ziebarth et al. (2020) find for their ROI is 800 MW as a central estimate. We extrapolate this power to 880 MW to account for the 10% increase of the ROI to the northwest. This collects nearly all components of our formulation of the extended paradox. Only the seismic efficiency $\bar{\eta}$ is left undefined after the preceding arguments. Here, the analysis of the fault-generated heat flow anomaly is decisive.

Lachenbruch and Sass (1980) argue that the upper bound to the heat flow anomaly generated by the San Andreas fault is 4.2–8.4 mW m^{-2} which they estimate to be caused by heat generation $\bar{Q}d$ on the fault of no more than 92 to 184 kW km^{-1}. We take the upper limit of this range, $\bar{Q}d = 184$ kW km^{-1}. By Equation 8, this leads to the following constraint:

$$P_H^{\mathrm{SAF}} \leq L \times \left(\bar{Q}d\right)_{\max} = L \times 184\mathrm{kW\,km^{-1}}. \tag{17}$$

Substituting the length of the SAF within the ROI, 625 km (see the marked fault trace in Figure 4), the upper limit on the frictional power on the investigated section of the SAF is hence

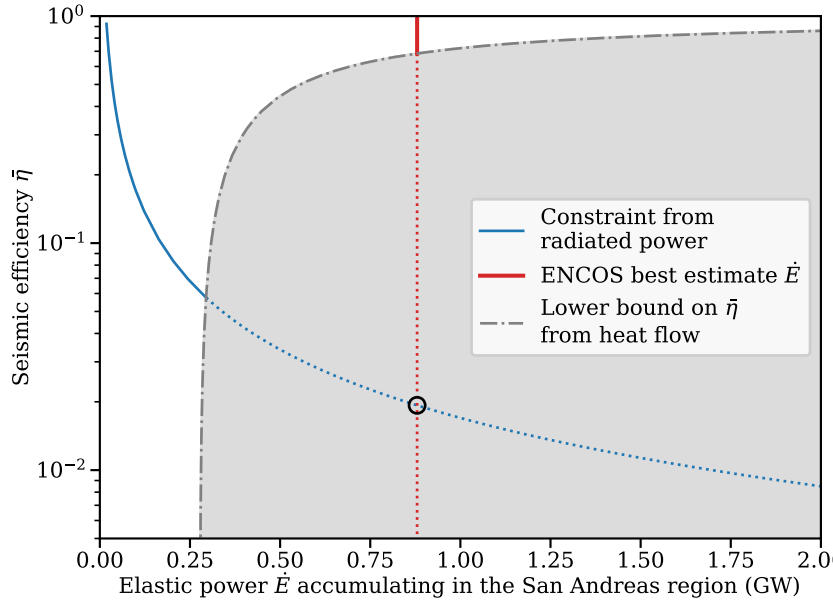

Figure 5. The extended paradox. The region of interest (ROI) is shown in Figure 3. The constraint for the radiated power in the ROI, $P_r = \bar{\eta}\dot{E}$ is shown for $P_r = 17$ MW computed from the earthquake catalogs, Equation 11 and Figure 4. The constraint on the input power $\dot{E}$ is shown for $\dot{E} = 880$ MW extrapolated from the result of Ziebarth et al. (2020). The lower bound on $\bar{\eta}$ follows from the heat flow constraint on the SAF by Lachenbruch and Sass (1980), Equation 20. The constraints on P_r and $\dot{E}$ meet in the area prohibited by the lower bound on $\bar{\eta}$ from the heat flow data (the two constraints are dashed within the exclusion zone).

$$P_H^{\mathrm{SAF}} \leq P_H^{\max} = 115\,\mathrm{MW}. \tag{18}$$

Through Equation 16, we now obtain the following constraint in the space of seismic efficiency $\bar{\eta}$ and elastic power $\dot{E}$ of the ROI

$$f(1-\bar{\eta})\dot{E} = P_H^{\mathrm{SAF}} \leq P_H^{\max} \tag{19}$$

that can be expressed as a lower bound on $\bar{\eta}$:

$$\bar{\eta} \geq \max\left\{1 - \frac{P_H^{\max}}{f\dot{E}}, 0\right\}. \tag{20}$$

The formulation of our extended paradox is now complete and Figure 5 illustrates it in the parameter space of seismic efficiency $\bar{\eta}$ and elastic power $\dot{E}$ of the ROI. The vertical red line shows the best estimate $\dot{E} = 880$ MW. The blue line shows the isoline $P_r = 17$ MW (Equation 11). The system should be parameterized by the parameter combination at the intersection of both lines, the black circle. Alas, this circle lies in the gray area in which the inequality Equation 20 is violated.

Clearly, one of the estimates based on our assumptions is incorrect. In the following sections, we explore four hypotheses that can reconcile the three constraints.

4. Discussion

4.1. Insufficient Effects

4.1.1. Seismic Moment Rate On and Off SAF

A first potential resolution to the extended paradox is the fraction ξ of radiated power within the ROI that is radiated on the SAF. In the derivation of the extended paradox, we have derived ξ from a joint earthquake catalog of the last 150–250 years. This catalog is not large enough to cover multiple return periods of the largest earthquakes in the region, and Figure 4b illustrates strikingly how just a few large earthquakes dominate the cumulative energy

of the catalog. The obtained ξ might hence be particularly susceptible to non-uniform return periods and our observation window.

As an alternate model for ξ, we have employed the UCERF3 model (Field et al., 2014; Milner, 2014). The UCERF3 model integrates a number of other data sources besides earthquake catalogs, such as paleoseismic observations of earthquake recurrence rates, fault slip rates, and geodetic deformation rates. The combination of these data sources in a joint inversion allows the model to estimate long-term seismicity rates on the faults.

The time-independent UCERF3 contains a set of rupture scenarios with associated moment magnitude and recurrence rate. The magnitudes can be converted to radiated energy using Equation 10 and then to radiated power by multiplying with the rupture's recurrence rate. Each rupture scenario is furthermore defined by the fault segments of the fault model that take part in it. Therefore, we can compute the model's radiated power from a fault by distributing all ruptures to the partaking fault segments and, for each segment, summing all contributions from different ruptures. In Text S1.2 in Supporting Information S1, we detail how we distribute the rupture powers and handle the logic tree.

When comparing the power radiated from the SAF trace in our ROI (Figure 4) with the remaining energy radiated from the ROI, we obtain a range of ξ from 22% to 43% with a median of 33%. Neither the median nor the minimum are small enough to shift the exclusion zone of Figure 5 to the intersection of the other two constraints (see also Figure S3 in Supporting Information S1). A value of ξ in the order of 10% would be required to resolve the extended paradox.

4.1.2. Radiated Power From Catalog

The same strong dependence on the 1857 Fort Tejon earthquake that affects ξ is also found in the computation of the radiated power P_r. As in the previous section, we have used UCERF3 as an alternate model of the long-term radiated power P_r. The computation, which is detailed in SI1.2 yields a radiated power 4–11 MW on the SAF in our ROI with a median $P_r = 7$ MW. Since this is lower than the radiated power derived from the catalogs ($P_r = 17$ MW), the P_r constraint curve in Figure 5 is shifted even further down and the extended paradox remains unresolved.

4.1.3. Scaled Energy

The scaled energy $e_r = E_r/M_0$ (e.g., Kanamori et al., 2020) affects, either directly or by being implied, all calculations in which energy is computed from seismic moment. In our case, this affects all estimates of radiated power P_r. Since the scaled energy is a linear factor, all estimates of the radiated power are linearly affected by uncertainty in e_r. Indeed, estimates of the scaled energy vary by orders of magnitude (Kanamori et al., 2020) so that this parameter is another candidate for the resolution of the extended paradox.

To resolve the extended paradox, the scaled energy has to be larger than the value we have used to compute Figure 5 so that the P_r curve is shifted upwards and intercepts the exclusion zone at an elastic power $\dot{E} >$ 880 MW. In our calculations, we have used conversion formulas based on the work of Kanamori (1977) which imply $e_r = 5 \times 10^{-5}$. Kanamori et al. (2020) list literature values of e_r up to 8×10^{-4} and derive, for their analyzed data set, values less than 10^{-4}. In our supplementary material SI1.1, we perform a statistical analysis of the scaled energy derived from the IRIS EQEnergy data product (M_0 and E_r estimates; IRIS DMC, 2013; Hutko et al., 2017) and from a number of studies (Baltay et al., 2014) and find that, where the result is not dominated by the prior choice, the scaled energy is less than 2×10^{-4} with 99% probability.

The result of these limits in scaled energy, both $e_r = 2 \times 10^{-4}$ or the rare event with $e_r = 8 \times 10^{-4}$, is that the extended paradox is not resolved. The P_r line intercepts the exclusion zone at 345 and 550 MW, respectively, and at seismic efficiencies of 20% and 50% (Figure S2b in Supporting Information S1). One of the other mechanisms to resolve the extended paradox would have to apply. If however a larger scaled energy is part of the extended paradoxes resolution, this implies that the efficiency of the SAF might be quite large.

4.2. Resolving the Extended Paradox

4.2.1. Hypothesis 1: Stochastic Fluctuations

The first resolution to the extended paradox we investigate is if a larger fault-generated heat flow anomaly might be allowed within the scatter of the heat flow data. If so, the heat flow constraint in Figure 5 shifts to the right, in

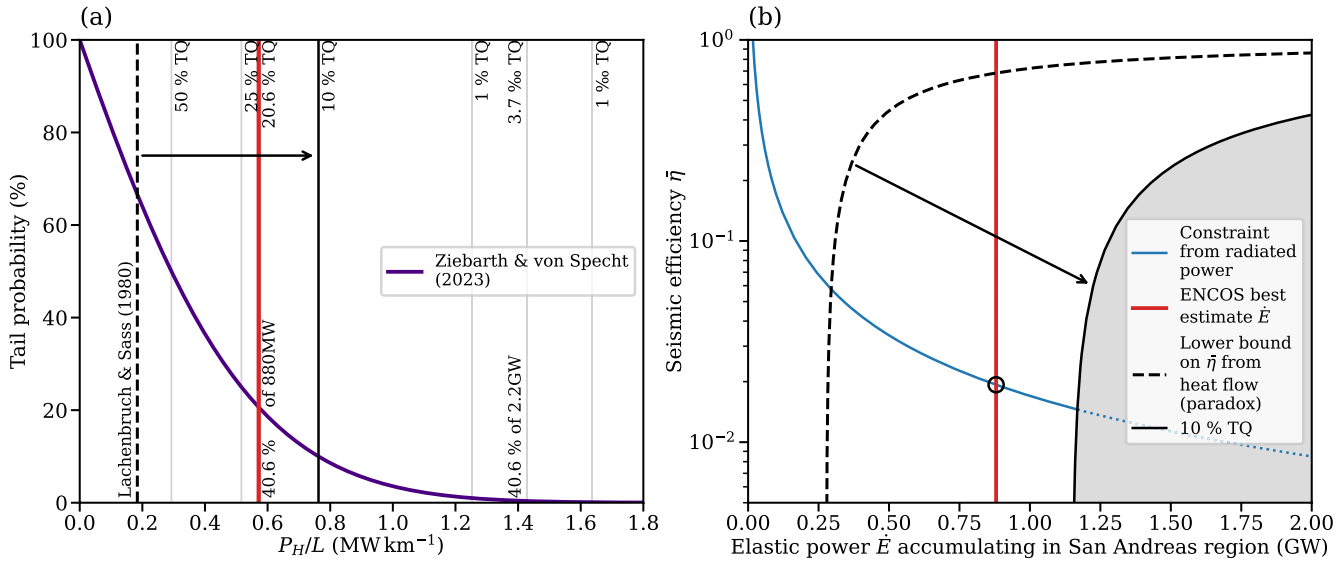

Figure 6. Resolving the extended paradox by considering heat flow fluctuations to be of stochastic origin. Panel (a) shows different solutions for the permissible heat flow anomaly strength on the selected parts of the SAF, expressed in frictional power per fault length. The dashed vertical line shows the upper bound that Lachenbruch and Sass (1980) assess, 0.2 × 0.92 MW km. The thick indigo line shows the posterior tail distribution that Ziebarth and von Specht (2023) derive for region (a) of Figure 3 using the REHEATFUNQ model. This curve denotes the posterior probability that the frictional power per fault length exceeds a given P_H/L under the assumption that heat flow fluctuations within the region are of stochastic origin. Multiple vertical lines indicate tail quantiles (TQ), that is, levels of the tail distribution. In particular, the circle of panel (b), that is, the point of the parameter space that conforms to the best estimate $\dot{E}$ of Ziebarth et al. (2020) and to P_r derived from the catalogs, corresponds to the thick vertical red line at 20.6% TQ. If we replace the upper bound on the anomaly strength from Lachenbruch and Sass (1980) by the 10% tail quantile of the statistical analysis, the constraint from P_r and $\dot{E}$ is within the upper bound. Panel (b) shows how the exclusion zone of Figure 5 transforms if we perform this step. The extended paradox is resolved. The ROI ("San Andreas region") is shown in Figure 3.

the direction to resolve the extended paradox. We use the method by Ziebarth and von Specht (2023) introduced in Section 2.4. Ziebarth and von Specht (2023) found that the most significant constraint of a SAF-generated heat flow anomaly can be derived for the Mojave section, region (a) in Figure 3. They used the heat flow anomaly (A23b) of Lachenbruch and Sass (1980), so their results are directly applicable to our question.

The heat flow anomaly quantification in the Mojave section results in the curve in Figure 6a, on which the horizontal axis is the frictional power per unit length of the fault, and the vertical axis is the probability that this frictional power, or larger, is consistent with the observed heat flow data.

Notably, the upper bound by Lachenbruch and Sass (1980) is below the median posterior frictional power. There is a considerable probability—about 70% taken at face value—that the anomaly could be of larger magnitude than their upper bound. Ziebarth and von Specht (2023) note that the central quantiles of the frictional power may be affected by deviations from their model assumptions, whose existence is unresolved. A central point estimate of the anomaly strength, for instance based on the median, may therefore not be reliable. The smaller posterior exceedance probabilities, on the other hand, are found to be resilient upper bounds on P_H even if heat flow does not follow their assumptions completely. Consequently, one might wish to choose, for instance, the 10% tail quantile as an upper bound of the anomaly strength and hence the frictional power. Figure 6b shows the heat flow constraint for the anomaly whose frictional power P_H is exceeded with 10% probability. Figure 7 illustrates heat flow anomalies corresponding to different frictional powers and probabilities next to the heat flow data.

Using the stochastic approach, the point of the $(\dot{E}, \bar{\eta})$-space that conforms to the elastic power constraint in Figure 5 has a 20.6% chance of being consistent with the heat flow data, where *consistency* means that a similar or larger heat flow anomaly were precluded by the scatter in the data. The extended paradox is resolved (Figure 6b) at about that probability.

The stochastic approach by Ziebarth and von Specht (2023) is a conservative way to interpret the heat flow data—considering each individual data point as a possible stochastic fluctuation and giving credence only to sets of measurements—and their modeling does not utilize all available information to disentangle the heat flow data. Further quality inspection of the individual heat flow data and corrections of physical effects, such as topography

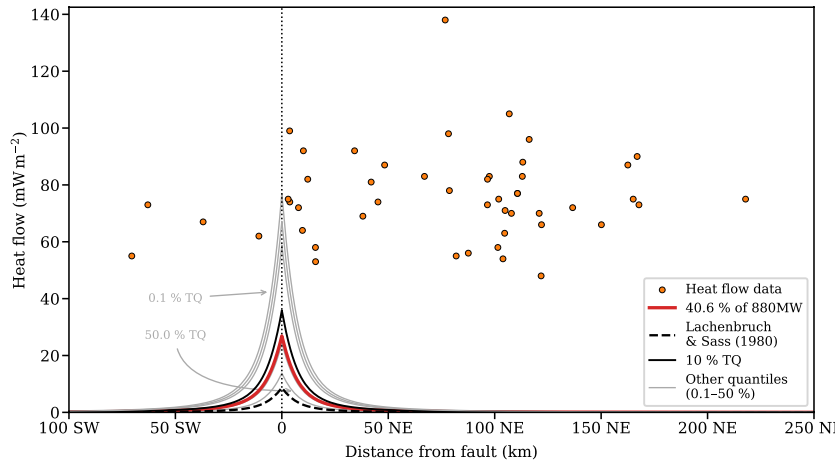

Figure 7. Statistically quantified heat flow anomaly compared with the heat flow data. The used heat flow data within region (a) of Figure 3 (there marked by stars) is plotted by distance from the fault trace. The fault-generated heat flow anomaly Equation 7 is shown for different powers P_H that correspond to the vertical lines shown in Figure 6a.

corrections (e.g., Blackwell et al., 1980; Fulton et al., 2004), are examples of information unused by the analysis of Ziebarth and von Specht (2023). Modeling the origin of large scale heat flow trends in the region, for instance due to slab window cooling (e.g., Popov et al., 2012), may be another example but care needs to be taken to base these kind of models on data that are independent from the heat flow data (which may not be possible).

By data detrending, data correction, or data subselection, this additional information may reduce the fluctuations of the heat flow data used in the analysis. This would tighten the statistical bounds on P_H, and nullify this first resolution of the extended paradox. Care then has to be taken to include effects of the heat flow detrending models that decrease our ability to discern the anomaly from the background. For instance, viscous dissipation that leads to a broadened heat flow anomaly (Takeuchi & Fialko, 2012) may lead to larger posterior P_H uncertainty since the diffuse signal may be more difficult to identify than the pointed anomaly Equation 7. Concludingly, hypothesis one shows that a stochastic interpretation can lead to drastically different results and should be considered when interpreting the heat flow data.

4.2.2. Hypothesis 2: Elastic Input Power Is Lower

A second resolution of the extended paradox we consider is the parameter uncertainty of the estimate of the elastic power $\dot{E}$. To resolve the extended paradox by means of adjusting $\dot{E}$, we need a low $\dot{E}$ to be plausible, so much as for the vertical line to fall left of the exclusion zone in Figure 5. Figure 8 sketches how a change in $\dot{E}$ can impact the power budget to resolve the extended paradox.

Ziebarth et al. (2020) investigate the uncertainty of their results by computing $\dot{E}$ for extreme choices of the parameters of their model. The two parameters of their model that yield the largest deviation toward a small elastic power are the static friction coefficient μ and the maximum depth $z_{\max}$ of the crustal volume that accumulates elastic energy to be released in earthquakes. The static friction coefficient μ controls, assuming a critically stressed crust, the magnitude of maximum differential stress within the crustal volume during the interseismic loading, and the depth $z_{\max}$ represents the lower boundary of that volume (i.e., the seismogenic crust). Both parameters μ and $z_{\max}$ factorize in the computation of $\dot{E}$ so that the maximum relative reduction of both parameters can be multiplied.

The lower end of the static friction coefficient μ considered by Ziebarth et al. (2020) reduces the elastic power within their ROI from 800 to 300 MW. The lower bound considered for $z_{\max}$ leads to a further ∼25% reduction. Combining both reductions, we obtain a lower bound of $\dot{E} \approx 250$ MW, which resolves the extended paradox (see Figure 9). However, each of them individually is not sufficient to resolve it.

The required parameter combination to resolve the extended paradox by means of the input power is quite extreme. The depth $z_{\max}$ would have to be 11 km throughout, which is in many places shallower than fault depths within the UCERF3 model, the seismogenic depth estimated by Zeng et al. (2022), and the estimated depth of the

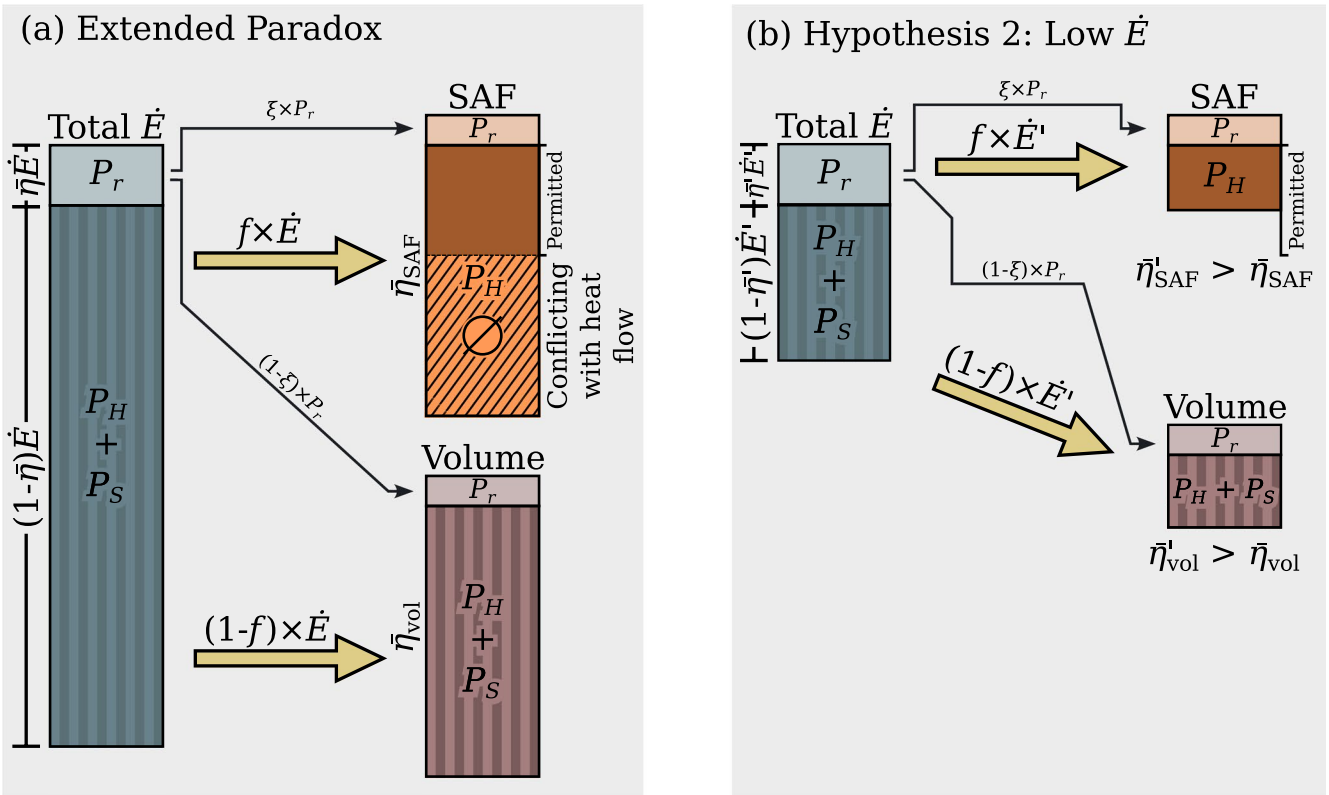

Figure 8. Sketch of hypothesis 2 to resolve the extended paradox of Section 3.2. Panel (a) illustrates the energy budget of the extended paradox. The total elastic input power $\dot{E}$, composed of radiated power P_r, frictional power P_H, and surface power P_S, is distributed between the SAF and the remaining volume according to the factor f. Surface power P_S is assumed possibly significant only in the remaining volume, where it is not distinguished from the frictional power. The total radiated power, given by the efficiency $\bar{\eta}$, is distributed between the SAF and the remaining volume according to the factor ξ. On the SAF, with $P_S = 0$, the surplus of the fractional $\dot{E}$ is frictional power P_H which is too large compared to the heat flow constraint. The hatched area shows the amount of P_H which is above the limit given by the heat flow data. Panel (b) shows how hypothesis 2 resolves the extended paradox. The total elastic input power $\dot{E}$ is reduced to $\dot{E}'$, but the values for the radiated energy P_r, ξ and f are the same as in panel (a). This results in an increase of the seismic efficiency $\bar{\eta}$. The reduced P_H on the SAF resolves the extended paradox.

brittle-ductile transition estimated by Cheng and Ben-Zion (2019). Furthermore, the static friction coefficient μ would have to be exceptionally low throughout the bulk volume, contradicting punctual in-situ measurements of stress magnitudes (e.g., at Cajon Pass; Townend & Zoback, 2000).

An alternative to the unlikely scenario that the static friction coefficient were small throughout all the bulk volume is that the differential stress is below criticality in the bulk volume assuming that a sufficiently large set of weak (low-μ) faults prevents the buildup of critical stresses in the bulk volume. Shebalin and Narteau (2017) present such a mechanism, a model of pore overpressure and plastic flow that leads to a low effective static friction coefficient in California along the SAF. We use their model to compute an effective static friction coefficient $\mu = 0.092$ that leads to the same depth-average stress at 16 km depth, where their model transitions to plastic flow (see Text S1.3 in Supporting Information S1). The configuration in Figure 9 goes below both parameters simultaneously.

The way that hypothesis two might be tested is by employing a more advanced, multidimensional geomechanical model that adheres to force balance. The need for a very low static friction coefficient μ in the model of Ziebarth et al. (2020) requires either the ubiquitous existence of pore overpressure or a sufficient number of statically weak faults that prevent the buildup of critical stress in the bulk crust. Townend and Zoback (2000) argue that widespread crustal pore overpressure is prevented by typical permeability of crustal rock, so that hypothesis two can be reduced to the question whether a very weak fault system could lead to a stress field in California that seems as if it were generated by a low static friction coefficient (0.08).

Existing geomechanical models that include the three-dimensional geometric setting and force balance generally support the existence of faults with low friction coefficients (e.g., Bird & Kong, 1994; Popov et al., 2012) that

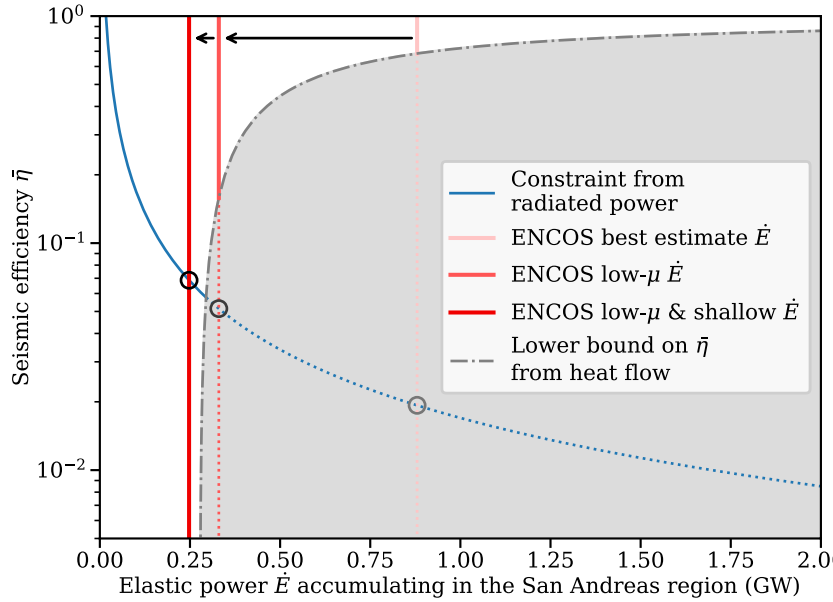

Figure 9. Resolving the extended paradox by using lower bounds on ENCOS $\dot{E}$. The best estimate elastic power $\dot{E} = 800$ MW of Ziebarth et al. (2020) scaled to our ROI is shown as a light red vertical line. Using $\dot{E}$ from the lowest static friction coefficient $\mu = 0.08$ that Ziebarth et al. (2020) have considered as extremal uncertainty, the constraint moves left as indicated by the long arrow. Using furthermore the lower end of the depth parameter z_{max}, the thickness of the energy-accumulating crust, the elastic power in our ROI is reduced to 250 MW and all three constraints can be fulfilled by the parameter combination indicated by the leftmost circle. The ROI ("San Andreas region") is shown in Figure 3.

would be required for the generally low stress field. What is more, these models typically require the existence of weak faults to reproduce the contemporary deformation data: Bird and Kong (1994) find best fit models with $\mu = 0.17$ and Popov et al. (2012) find a best-fit model with $\mu = 0.08$ on faults. Evaluating these kind of models for the regional strain rate and stress fields while using information about the contemporary fault system (as for instance done by Liu et al. (2010)) and computing the elastic input power $\dot{E}$ may be a way to test hypothesis two.

4.2.3. Hypothesis 3: Efficiency on SAF Differs From Volume

The third hypothesis is to relax the assumption that the efficiency on the SAF is the same as within the rest of the volume ($\bar{\eta} = \bar{\eta}_{SAF}$). This assumption implied that the distribution of radiated energy between SAF and volume is the same as the distribution of elastic input energy between the two ($\xi = f$; Equation 14). Consequently, in this section we consider $\xi \neq f$. Since the heat flow observations require the frictional power on the SAF to be low, a larger efficiency is needed on the SAF to resolve the extended paradox. Therefore in this section we have $\bar{\eta}_{SAF} > \bar{\eta}$ and $\xi > f$.

Relaxing the assumption $\bar{\eta} = \bar{\eta}_{SAF}$ decouples the total elastic power $\dot{E}$ from the frictional power P_H^{SAF} on the SAF. The frictional power within the rest of the volume can absorb all additional elastic power put into the volume without affecting the heat production and radiation on the SAF. Figure 10 illustrates the decoupling. In both panel (a) and (b), the radiated power distributes in the same manner between the SAF and the remaining volume (say $\xi = 41\%$ from the extended paradox). Furthermore, the total input power $\dot{E}$ is the same in both panels. Meanwhile, a large part of the frictional power assigned to the SAF in the extended paradox (panel a) is reassigned to the faults of the remaining volume in hypothesis 3. In this way, the frictional power on the SAF is low enough not to conflict with the constraint from heat flow data.

It is unlikely that a redistribution of frictional power from the SAF (Figure 10a) to all remaining faults of the volume (Figure 10b) would lead to a measurable heat flow anomaly elsewhere. The combined length of the remaining faults is considerably larger—additional known faults of roughly 10,000 km cumulative length are listed within the ROI by the UCERF3 model alone—and they are at least partly younger than the SAF. Thereby, heat flow anomalies along the remaining faults would be weaker than an anomaly on the SAF of the same frictional power, which, as laid out in Section 4.2.1, is already difficult to detect. Furthermore, our assumption

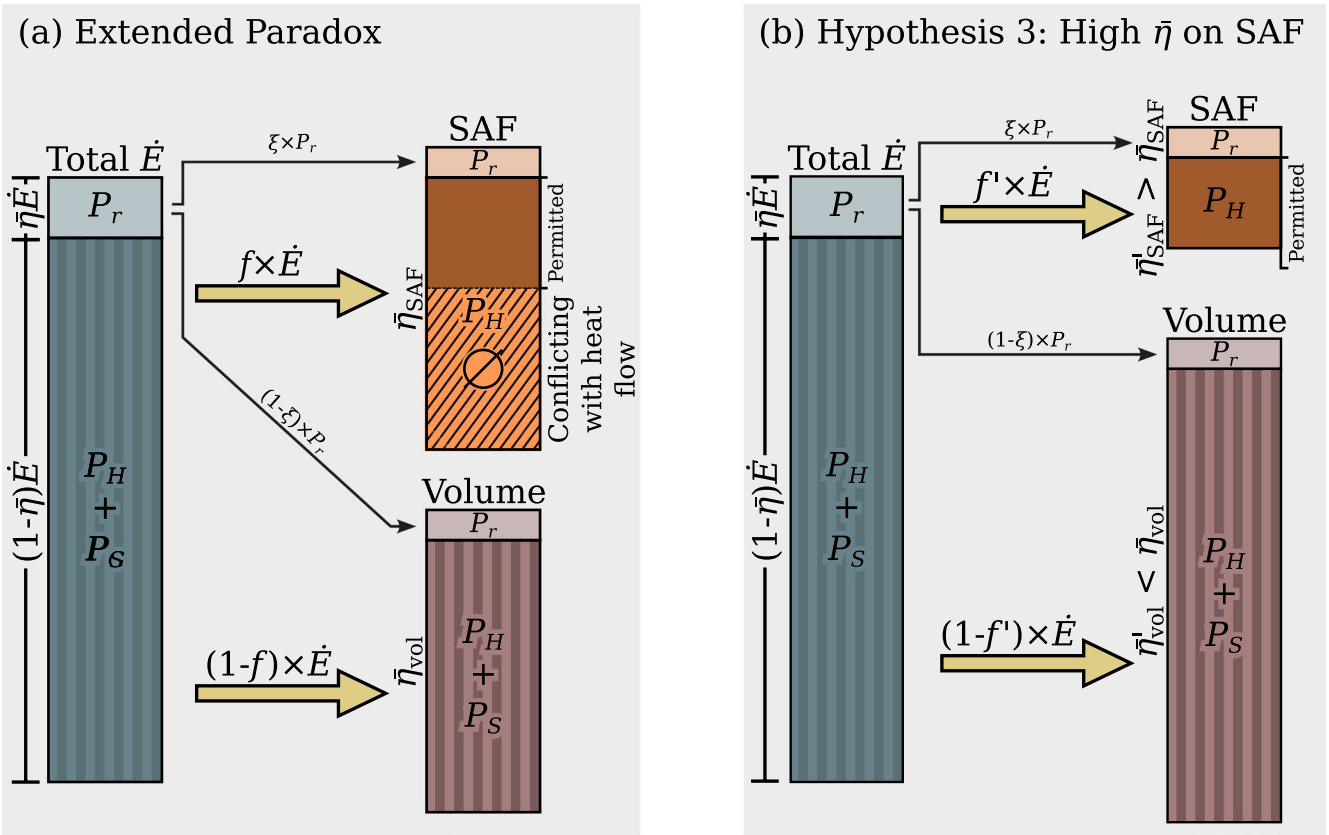

Figure 10. Sketch of hypothesis 3 to resolve the extended paradox. Panel (a) shows the energy budget in the extended paradox (see Figure 8). Panel (b) shows how hypothesis 3 resolves the extended paradox. The total seismic efficiency and elastic power are kept the same as in (a), and so is the distribution of P_r between SAF and remaining volume (ξ). The seismic efficiency $\bar{\eta}_{SAF}$ of the SAF is assumed to be higher than the efficiency $\bar{\eta}_{vol}$ in the rest of the volume, but $\dot{E}$, P_r and ξ do not change. This results in a decrease of the frictional power of the SAF. The remaining part of the frictional power is accounted for in the remaining volume's budget, leading to a lower seismic efficiency $\bar{\eta}'_{vol}$ compared to panel (a). An implication is that f' in panel (b) is smaller than f in panel (a).

of negligible surface energy in the power budget of the well-developed SAF cannot easily be transferred to the remaining faults in the volume. This could allow for a significant amount of surface energy in the power budget of the remaining volume, further reducing the frictional power available on each fault to generate the heat flow anomaly.

The relaxation of the homogeneity of the seismic efficiency has profound consequences for the parameter space of total elastic power and seismic efficiency if the efficiency on and off the SAF is allowed to vary arbitrarily. Then, the upper bound P_H^{max} on the frictional power on the SAF from the heat flow data (Equation 18) does not lead to an exclusion zone like in Figure 5. The underlying reason is that the power P_H on the SAF could always be lowered into the permitted range (Figure 10b) by increasing the seismic efficiency on the SAF. Instead, the heat flow constraint on the frictional power leads to an upper bound on the total radiated power. Vice versa, a given total radiated power leads to a lower bound for the efficiency on the SAF.

We now derive these bounds. Using Equations 3 and 4 for the power budget on the SAF and expressing the radiated power on the SAF through ξ and P_r (Equation 12), we get

$$P_H^{SAF} = (1-\bar{\eta}_{SAF})\frac{P_r^{SAF}}{\bar{\eta}_{SAF}} = \frac{1-\bar{\eta}_{SAF}}{\bar{\eta}_{SAF}}\xi P_r \le P_H^{max}, \tag{21}$$

which inserted into the inequality Equation 18 leads to the upper bound

$$P_r = \bar{\eta}\dot{E} \le \frac{\bar{\eta}_{SAF}}{(1-\bar{\eta}_{SAF})\xi}P_H^{max}. \tag{22}$$

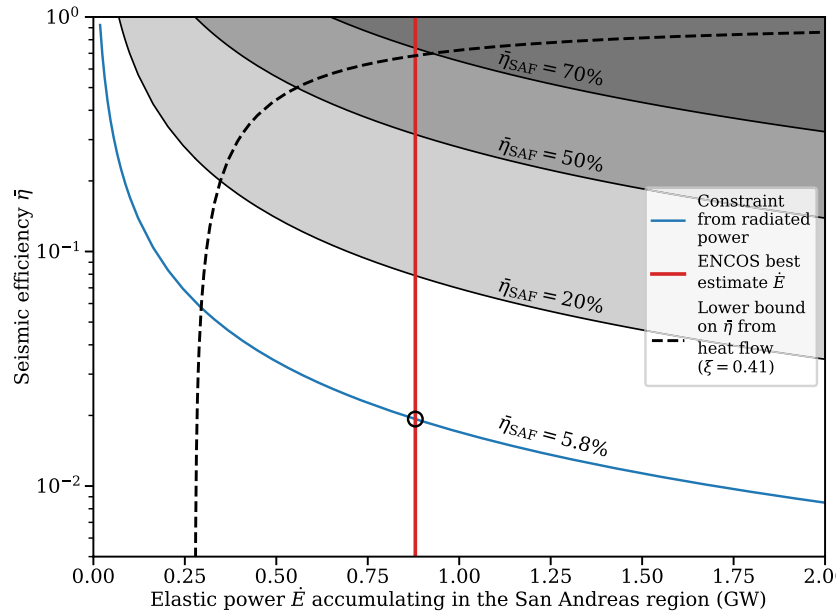

Figure 11. Resolving the extended paradox by larger seismic efficiency on the San Andreas fault. The change of the exclusion zones of Figure 5 is illustrated when the fraction of radiated power ξ is not equal to the fraction f of elastic power on the SAF, both relative to the respective power in the volume. The gray shaded areas show areas of the parameter space that are forbidden due to the heat flow constraint on the frictional power on the SAF, Equation 22. The ROI ("San Andreas region") is shown in Figure 3.

Figure 11 illustrates this upper bound for a number of seismic efficiencies on the SAF. Beginning at

$$\bar{\eta}_{SAF} \geq \frac{P_r \xi}{P_r \xi + P_H^{max}} = 5.8\,\%, \tag{23}$$

the three constraints on $\bar{\eta}$ and $\dot{E}$ can be fulfilled simultaneously and the extended paradox is resolved.

This particular value for the average seismic efficiency, 5.8%, is plausible. Not many estimates of the seismic efficiency have been computed for natural earthquakes since the total energy ΔE released during an earthquake cannot be inferred by seismological means (e.g., Wang, 2004). Additional data needs to be available to estimate the frictional dissipation during the earthquake. McGarr (1976) has analyzed mining-induced earthquakes in which ΔE can be estimated from the collapsed volume and found seismic efficiencies in the range of 0.1–1.0%. McGarr (1999) conjectured that $\eta \leq 6\%$ is an upper bound for the seismic efficiency, coinciding with the seismic efficiency of laboratory stick-slip earthquakes by Lockner and Okubo (1983) in which $4\% \leq \eta \leq 8\%$. Noting that the upper bound of this conjecture has been challenged to be too low (Ide & Beroza, 2001; Wang, 2004), our lower bound of 5.8% is clearly plausible. An interesting observation comparing our lower bound with the results presented by McGarr (1999) is that in this hypothesis, the SAF must be more efficient than the earthquakes observed by McGarr (1976)—which might correspond to less active faults—but the stick-slip process observed by Lockner and Okubo (1983) would be sufficiently efficient.

Kanamori and Heaton (2000) present a model for large earthquakes that allows large seismic efficiencies and can hence fulfill Equation 23. The key component that leads to high seismic efficiencies is a dynamic weakening of the fault due to thermal effects that becomes relevant for large earthquakes. The resulting low coseismic friction and fault-generated heat flow has been observed in Taiwan and Japan (Fulton et al., 2013; Kano et al., 2006). Multiple different mechanisms have been proposed for the dynamic weakening, such as dynamic pore overpressure (Kanamori & Heaton, 2000; Sibson, 1973), flash heating (e.g., Goldsby & Tullis, 2011; Kanamori & Heaton, 2000), and "wrinkle-like slip pulses" (Andrews & Ben-Zion, 1997, this effect is not thermal). Thermal dynamic weakening effects have been numerically simulated by Lambert et al. (2021), who find that in statically strong faults, they can lead to "self-healing pulse-like" ruptures with high seismic efficiencies (judging from their Figure 2c).

Testing the plausibility of hypothesis 3 is elaborate. Deriving the average efficiency of the SAF from observed earthquakes is prohibited by the return time of large earthquakes. What remains is to assess the plausibility of potential mechanisms for a high seismic efficiency. Scholz (2006) outlines arguments to reject multiple mechanisms that could cause coseismic friction. A rigorous quantitative review of these arguments may help test hypothesis 3. Furthermore, large-scale computational models of coseismic dynamics on and off the fault may help to test wave-theoretic models (e.g., Andrews & Ben-Zion, 1997).

The explanatory power of the heat flow analysis for the volume's parameters can be restored if a lower bound on the seismic efficiency within the rest of the volume could be stated. This way, the frictional power in the volume could not simply grow without bounds and at a point, the radiated power in the remaining volume and (due to fixed ξ) the other powers of the budget shown in Figure 10b would have to increase to accommodate a growth in total elastic power. This, in turn, would bring the frictional power P_H^{SAF} on the SAF closer to its maximum permitted by the heat flow analysis.

4.2.4. Hypothesis 4: Low Scaled Energy on SAF ($\xi = f$ Small)

The final hypothesis we consider is that the scaled energy e_R, the ratio of radiated energy to seismic moment, is fault-dependent and smaller on the SAF than in the remaining volume. Previously in Section 4.1.3, we have shown that although the scaled energy directly affects all our estimates of radiated power from seismic moment, a uniform change of e_R across the ROI cannot resolve the extended paradox within the currently known range of e_R. The same, however, need not hold if the scaled energy differs on a fault-basis rather than spatially uniformly. In particular this might have an impact if the SAF as a well-developed fault hosts earthquakes of different scaled energy than the remaining faults.

A change in scaled energy can help resolve the extended paradox if it leads to a sufficiently reduced P_H on the SAF. The scaled energy has a direct control foremost on the radiated power P_r, hence a difference of e_R between the SAF and the volume changes ξ first. Yet, in the derivation of the extended paradox in Section 3.2, we have assumed that the elastic power is distributed in the same ratio on and off the SAF as the radiated power, $f = \xi$. To distinguish hypothesis 4 from hypothesis 3, we retain the equality of the seismic efficiency on and off the SAF, and hence vary $f = \xi$ simultaneously. Consequently, we look at f and ξ smaller than the value of 41% of Section 3.2 to resolve the extended paradox. Figure 12 sketches the changes in power budget that result from hypothesis 4.

Smaller values of ξ and f can be obtained for a given seismic moment rate if the scaled energy on the SAF is lower than on the remaining faults. Suppose that the scaled energy on the SAF is lower by a factor g than in the surrounding volume $\left(e_R^{\mathrm{SAF}} = g e_R^{\mathrm{vol}}\right)$. Then we can express ξ by g and the moment rates on the SAF and within the volume:

$$\xi = \frac{g \dot{M}_0^{\mathrm{SAF}}}{g \dot{M}_0^{\mathrm{SAF}} + \dot{M}_0{}^{\mathrm{vol}}}. \tag{24}$$

To determine how small g can plausibly be, we have evaluated the distribution of scaled energy from a number of sources (Baltay et al., 2014; IRIS DMC, 2013; Kanamori et al., 2020, see Text S1.1 in Supporting Information S1) and found that 90% of the scaled energy estimates are contained in the interval 5×10^{-6} to 6×10^{-5}. If we assume that e_R on the SAF is at the low end and the remaining volume at the high end of this range, we obtain $f = \xi = 5.6\%$ by repeating the catalog analysis of Section 3.2.

These values of ξ and f can resolve the extended paradox. Figure 13 shows the resulting exclusion zone, which is shifted to larger powers with more than twice the elastic power $\dot{E}$ of the best estimate of Ziebarth et al. (2020) permitted. We also computed the approximate f, 13%, at which the extended paradox is just resolved due to low f. The resulting exclusion zone is shown as a dashed line in Figure 13. This f (and ξ) is obtained if the scaled energy is a factor 4.7 lower on the SAF than on the remaining faults of the volume.

A key question for the validity of this last hypothesis is whether the systematic factor five difference in scaled energy between the SAF and the remaining faults of the volume is possible. Compared to the event-to-event variability, most contemporary studies find only mild correlation of the scaled energy with tectonic regime (see e.g., Baltay et al., 2014; Denolle & Shearer, 2016; Kanamori et al., 2020) and no significant dependency on magnitude (e.g., Baltay et al., 2011; Denolle & Shearer, 2016; Kanamori et al., 2020). One exception are large interplate earthquakes in subduction zones that show systematically lower scaled energy (Denolle & Shearer, 2016).

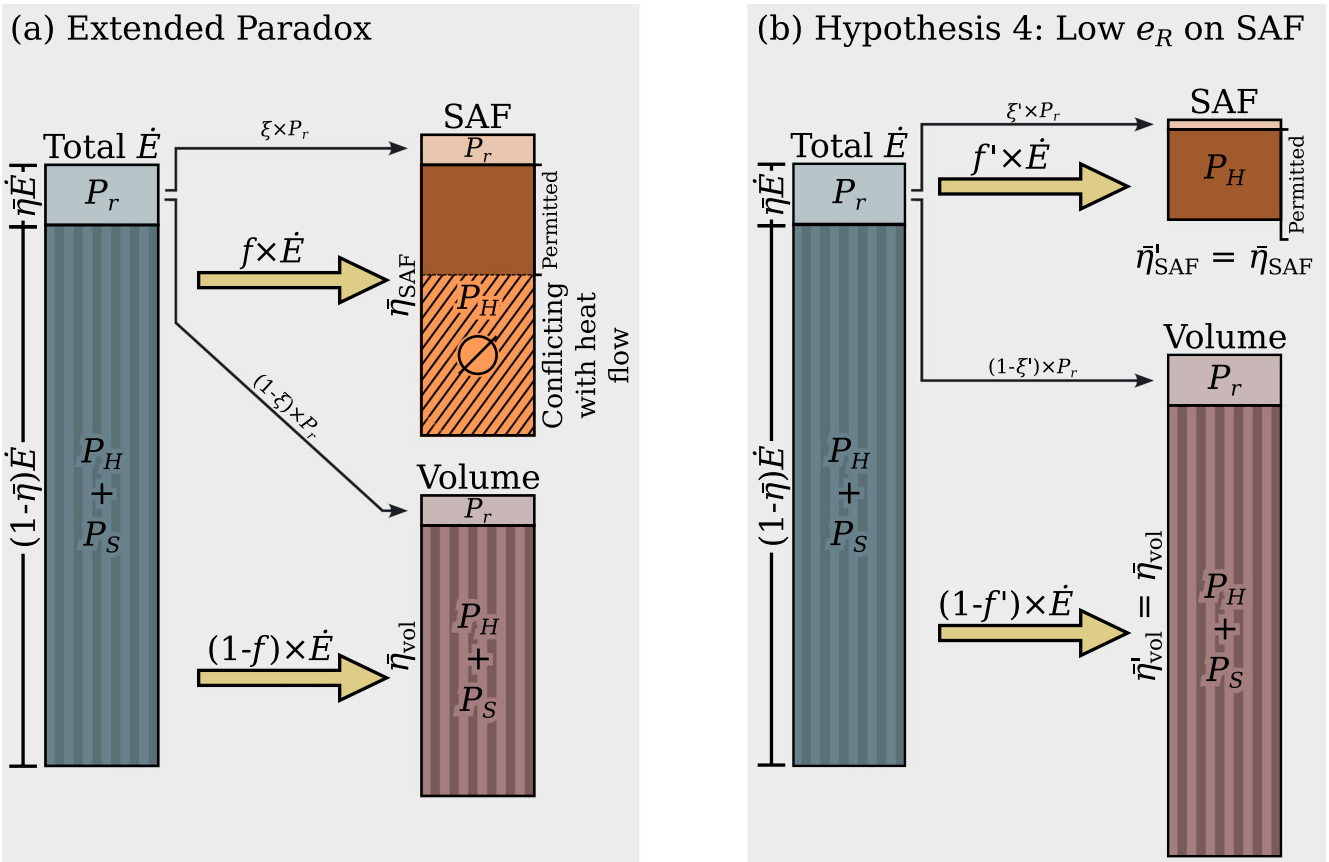

Figure 12. Sketch of hypothesis 4 to resolve the extended paradox. Panel (a) shows the energy budget in the extended paradox (see Figure 8). Panel (b) shows how hypothesis 4 resolves the extended paradox. The partition of P_r and $\dot{E}$ between SAF and remaining volume (ξ and f) are reduced simultaneously ($\xi = f$). The seismic efficiency and total elastic power do not change. This scenario would result from a scaled energy e_R that is lower on the SAF than on the other faults of the volume under the constraint of a homogeneous seismic efficiency. Resulting from the smaller f, frictional power on the SAF is reduced, resolving the extended paradox.

Denolle and Shearer (2016) list averages of the scaled energy for intra- and interplate earthquakes that differ by a factor of 6.7, which would be compatible with the required factor 5 if the SAF were similar to a subduction plate boundary.

Radiguet et al. (2009) find from the analysis of 28 large continental earthquakes that the ground shaking originating from immature faults is on average 1.5 times larger than that from mature faults, suggesting that the scaled energy differs by a factor of 2. This is insufficient for the required factor 5. Among the earthquakes Radiguet et al. (2009) analyzed is a single data point for the SAF, the 2004 *M*6 Parkfield earthquake, suggesting a contradiction with hypothesis 4 if this data point were representative for the SAF. However, in a recent study Guo et al. (2023) find that the scaled energy may depend non-monotonously on the geological maturity of the fault, with peak scaled energy at intermediate maturity and lower scaled energy at low and high maturity. They propose increased energy dissipation in fracture growth for the very immature, and lack of high-frequency radiation in mature faults as mechanisms for this dependency. Within their set of 34 investigated earthquakes, the scaled energy ranges roughly within a factor 9. This might allow for sufficient systematic variation of the scaled energy between the San Andreas fault and less mature faults, although there is considerable scatter that prevents a clear systematic estimate.

In light of the sparse data situation, hypothesis 4 cannot yet be tested. Its clarification depends on whether the SAF as a plate boundary is, on average, similar in scaled energy to subduction zones, or whether its average scaled energy is more similar to the average intraplate fault. The study of Guo et al. (2023) might, in conjunction with a detailed study of the seismic moment rate distribution across the Southern Californian fault system, be a promising starting point for future tests of this hypothesis 4.

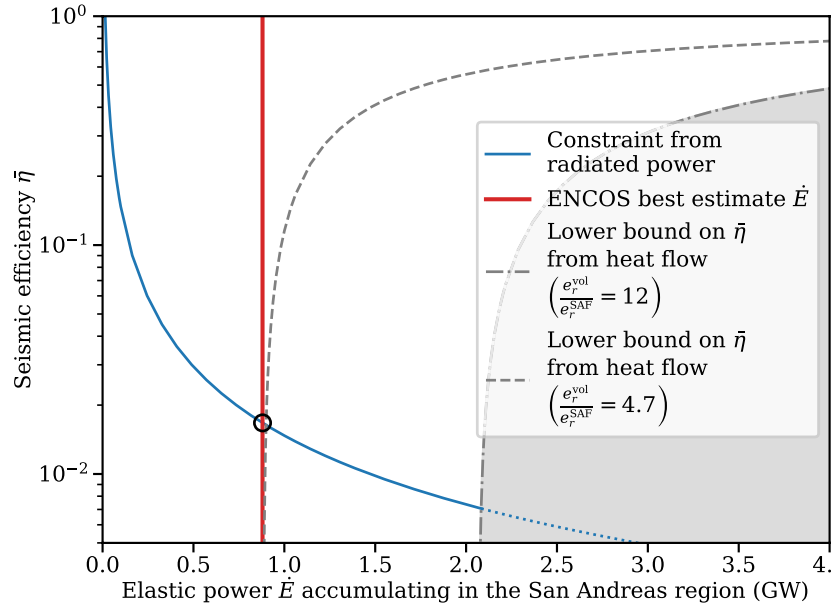

Figure 13. Resolving the extended paradox by a weak low-radiation mature fault. The proposed fault has a low scaled energy e_R due to a low static coefficient of friction μ. It releases less elastic power at a given slip rate and hence has a smaller f. The filled exclusion zone has $f = 5.6\%$ and the dashed line shows $f = 13\%$. We keep the equality $\xi = f$ intact. The ROI ("San Andreas region") is shown in Figure 3.

4.3. Combined Hypotheses and Implications for Seismic Hazard

The four hypotheses we discussed have been chosen to be simple in the energy-related parameters of the extended paradox. Each hypothesis focuses on the effect that one relevant parameter can have on the extended paradox, and in a sense can be called an end-member of the problem. Our set of hypotheses lists all relevant mechanisms to resolve the extended paradox under the assumptions we have taken, and in the energy-related parameters.

At least some of the parameter changes of the hypotheses can be combined and reality might be a mixture of some end-members. For instance, the SAF could be very efficient but the remaining weak heat flow anomaly hidden by heat flow fluctuations. Another example is the "crack-like" rupture model by Lambert et al. (2021), which produces earthquakes of low scaled energy (hypothesis 4) but simultaneously operates at generally low differential stresses (hypothesis 2).

The distinction between these mechanisms is important for the assessment of seismic hazard. Hypotheses 1–3, for instance, yield higher radiated power on the SAF compared to the remaining volume than hypothesis 4, while the inverse is true for the remaining volume. Further inspection of the limits of the parameters—in particular the scaled energy on and off the SAF—seems warranted in this context. The extended paradox provides a constraining context for further work.

Finally, the heat flow constraints on the frictional power can be used to constrain the parameter space of elastic power and seismic efficiency. The exclusion zone shown in Figure 5 removes a chunk of the parameter space of $\dot{E}$ and $\bar{\eta}$ for $\dot{E} \leq 2$ GW. These parameters are crucial components of the seismicity model of Ziebarth et al. (2020). The exclusion zone has the potential to yield information that adds to the estimate of the elastic power $\dot{E}$ (excluding the dotted part of the vertical line in Figure 5), constraining the seismic efficiency from below and hence leading to a minimum radiated power.

5. Conclusions

Translating the San Andreas heat flow paradox to the parameter space of accumulating elastic power and seismic efficiency, and augmenting it with recent estimates of the input power in Southern California (Ziebarth et al., 2020) leads to the extended paradox. Well-known bounds on the strength of a fault-generated heat flow anomaly across the San Andreas fault (Lachenbruch & Sass, 1980) lead to a constraint on the fault's frictional power that is not compatible with the radiated power and the elastic power in the region.

Four escape routes can resolve the extended paradox. First, a stochastic interpretation of the heat flow variability within the region finds a 20% probability that a fault-generated heat flow anomaly consistent with the radiated and input power of the region exists. Second, within the uncertainties the elastic input power in Southern California might be small enough to resolve the extended paradox; this would require an exceptionally low static friction coefficient ($\mu = 0.08$) and thickness of the energy-accumulating crust ($z_{\max} = 11$ km). Third, the San Andreas fault might differ from the remaining faults in the system by a comparatively high seismic efficiency ($\bar{\eta} \geq 5.8\,\%$). Fourth, the San Andreas might be a weak mature fault characterized by a low scaled energy E_r/M_0, one fifth of the surrounding volume. Finally, a combination of multiple hypotheses can also resolve the extended paradox.

The methodology we have developed in this work has useful implications not only to understand the long-term energy budget of the SAF but also for the analysis of seismic hazard. The use of the heat flow data leads to a further, probabilistic constraint in the space of seismic efficiency and elastic power, two key parameters of long-term seismicity modeling in energy space (Ziebarth et al., 2020). The constraint is complementary to existing information derived from other types of data. The use of an energy-based framework, in turn, can be beneficial for the quantification of shaking and seismic hazard (Picozzi et al., 2018; Ziebarth et al., 2020).

Conflict of Interest

The authors declare no conflicts of interest relevant to this study.

Data Availability Statement

The heat flow data used in this study are available in the online supplement of Lucazeau (2019). Shorelines in the maps are from the GSHHS (Wessel & Smith, 1996, 2017). The UCERF3 model can be downloaded from Milner (2014). The earthquake catalogs are available from Felzer and Cao (2008) and Cheng et al. (2023a). All waveform and parametric data for the latter are available from the Southern California Seismic Network (Caltech & USGS, 1932); stored at the Southern California Earthquake Data Center (USGS & SCEC, 1991).

Shorelines are derived from the OpenStreetMap database available under the Open Database License and can be downloaded from The OpenStreetMap Contributors (2023).

Code to evaluate the heat flow posterior is archived at GFZ Data Services (Ziebarth, 2023c). Code to evaluate the radiated power from the UCERF3 model is available from Ziebarth (2023a). Code used to evaluate the distribution of the scaled energy is available from Gardini et al. (2022) and Ziebarth (2023b). Other computations performed in this work use NumPy (The NumPy Contributors, 2023; van der Walt et al., 2011) and SciPy (The SciPy Contributors, 2023; Virtanen et al., 2020). Some geodesic distance computations have been performed using the GeographicLib library (Karney, 2018).

Acknowledgments
MJZ would like to thank J. Brune for helpful and enlightening discussions during the development of this manuscript. The authors are grateful to editor Yves Bernabé, the anonymous associate editor, and the anonymous reviewers for valuable feedback that helped us improve our manuscript. This work has received funding from the Initiative and Networking Fund of the Helmholtz Association through the project Advanced Earth System Modelling Capacity (ESM). Open Access funding enabled and organized by Projekt DEAL.

References

Anderson, D. L. (1971). The San Andreas fault. *Scientific American*, *225*(5), 52–68. https://doi.org/10.1038/scientificamerican1171-52

Anderson, J. G. (1979). Estimating the seismicity from geological structure for seismic-risk studies. *Bulletin of the Seismological Society of America*, *69*(1), 135–158.

Andrews, D. J., & Ben-Zion, Y. (1997). Wrinkle-like slip pulse on a fault between different materials. *Journal of Geophysical Research*, *102*(B1), 553–571. https://doi.org/10.1029/96JB02856

Baltay, A. S., Beroza, G. C., & Ide, S. (2014). Radiated energy of great earthquakes from teleseismic empirical green's function deconvolution. *Pure and Applied Geophysics*, *171*(10), 2841–2862. https://doi.org/10.1007/s00024-014-0804-0

Baltay, A. S., Ide, S., Prieto, G., & Beroza, G. (2011). Variability in earthquake stress drop and apparent stress. *Geophysical Research Letters*, *38*(6), L06303. https://doi.org/10.1029/2011GL046698

Bird, P., & Kong, X. (1994). Computer simulations of California tectonics confirm very low strength of major faults. *GSA Bulletin*, *106*(2), 159–174. https://doi.org/10.1130/0016-7606(1994)106⟨0159:CSOCTC⟩2.3.CO;2

Bird, P., Kreemer, C., & Holt, W. E. (2010). A long-term forecast of shallow seismicity based on the global strain rate map. *Seismological Research Letters*, *81*(2), 184–194. https://doi.org/10.1785/gssrl.81.2.184

Blackwell, D. D., Steele, J. L., & Brott, C. A. (1980). The terrain effect on terrestrial heat flow. *Journal of Geophysical Research*, *85*(B9), 4757–4772. https://doi.org/10.1029/JB085iB09p04757

Brune, J. N., Henyey, T. L., & Roy, R. F. (1969). Heat flow, stress, and rate of slip along the San Andreas fault, California. *Journal of Geophysical Research*, *74*(15), 3821–3827. https://doi.org/10.1029/JB074i015p03821

Byerlee, J. (1978). Friction of rocks. *Pure and Applied Geophysics*, *116*(4), 615–626. https://doi.org/10.1007/BF00876528

Cacace, M., Scheck-Wenderoth, M., Noack, V., Cherubini, Y., & Schellschmidt, R. (2013). Modelling the surface heat flow distribution in the area of Brandenburg (northern Germany). *Energy Procedia*, *40*, 545–553. (European Geosciences Union General Assembly 2013, EGUDivision Energy, Resources & the Environment, ERE). https://doi.org/10.1016/j.egypro.2013.08.063

Caltech, & USGS. (1932). Southern California seismic network (SCSN). https://doi.org/10.7914/SN/CI
Cheng, Y., & Ben-Zion, Y. (2019). Transient brittle-ductile transition depth induced by moderate-large earthquakes in Southern and Baja California. *Geophysical Research Letters*, *46*(20), 11109–11117. https://doi.org/10.1029/2019GL084315
Cheng, Y., Hauksson, E., & Ben-Zion, Y. (2023a). Focal mechanism catalog for Southern California [Dataset]. Mendeley Data. (V5.). https://doi.org/10.17632/9s54cy253d.5
Cheng, Y., Hauksson, E., & Ben-Zion, Y. (2023b). Refined earthquake focal mechanism catalog for southern California derived with deep learning algorithms. *Journal of Geophysical Research: Solid Earth*, *128*(2), e2022JB025975. https://doi.org/10.1029/2022JB025975
Cheng, Y., Ross, Z. E., Hauksson, E., & Ben-Zion, Y. (2021). A refined comprehensive earthquake focal mechanism catalog for southern California derived with deep learning algorithms (No. S32A-05). (presented at 2021 Fall Meeting, AGU, 15 Dec).
Christophersen, A., & Gerstenberger, M. C. (2021). Expert judgement for geological hazards in New Zealand. In A. M. Hanea, G. F. Nane, T. Bedford, & S. French (Eds.), *Expert judgement in risk and decision analysis* (pp. 345–371). Springer International Publishing. https://doi.org/10.1007/978-3-030-46474-5_15
Cocco, M., Aretusini, S., Cornelio, C., Nielsen, S. B., Spagnuolo, E., Tinti, E., & Di Toro, G. (2023). Fracture energy and breakdown work during earthquakes. *Annual Review of Earth and Planetary Sciences*, *51*(1), 217–252. https://doi.org/10.1146/annurev-earth-071822-100304
Crank, J. (1975). *The mathematics of diffusion* (2nd ed.). Clarendon Press.
Dahlen, F. A. (1977). The balance of energy in earthquake faulting. *Geophysical Journal International*, *48*(2), 129–161. https://doi.org/10.1111/j.1365-246X.1977.tb01298.x
Denolle, M. A., & Shearer, P. M. (2016). New perspectives on self-similarity for shallow thrust earthquakes. *Journal of Geophysical Research: Solid Earth*, *121*(9), 6533–6565. https://doi.org/10.1002/2016JB013105
Drury, M. J. (1987). Thermal diffusivity of some crystalline rocks. *Geothermics*, *16*(2), 105–115. https://doi.org/10.1016/0375-6505(87)90059-9
Felzer, K. R., & Cao, T. (2008). *WGCEP historical California earthquake catalog, appendix H in the uniform California earthquake rupture forecast, version 2 (UCERF2)* (p. 127). U.S. Geological Survey Open-File Report 2007-1437H and California Geological Survey Special Report 203H. Retrieved from http://pubs.usgs.gov/of/2007/1437/h/
Field, E. H., Arrowsmith, R. J., Biasi, G. P., Bird, P., Dawson, T. E., Felzer, K. R., et al. (2014). Uniform California earthquake rupture forecast, version 3 (UCERF3)—The time-independent model. *Bulletin of the Seismological Society of America*, *104*(3), 1122–1180. https://doi.org/10.1785/0120130164
Fulton, P. M., Brodsky, E. E., Kano, Y., Mori, J., Chester, F., Ishikawa, T., et al. (2013). Low coseismic friction on the Tohoku-Oki fault determined from temperature measurements. *Science*, *342*(6163), 1214–1217. https://doi.org/10.1126/science.1243641
Fulton, P. M., Saffer, D. M., Harris, R. N., & Bekins, B. A. (2004). Re-evaluation of heat flow data near Parkfield, CA: Evidence for a weak San Andreas fault. *Geophysical Research Letters*, *31*(15), L15S15. https://doi.org/10.1029/2003GL019378
Gardini, A., Fabrizi, E., & Trivisano, C. (2022). Bayesian inference for log-normal data [Software]. Retrieved from https://cran.r-project.org/package=BayesLN
Goldsby, D. L., & Tullis, T. E. (2011). Flash heating leads to low frictional strength of crustal rocks at earthquake slip rates. *Science*, *334*(6053), 216–218. https://doi.org/10.1126/science.1207902
Goutorbe, B., Poort, J., Lucazeau, F., & Raillard, S. (2011). Global heat flow trends resolved from multiple geological and geophysical proxies. *Geophysical Journal International*, *187*(3), 1405–1419. https://doi.org/10.1111/j.1365-246X.2011.05228.x
Guo, H., Lay, T., & Brodsky, E. E. (2023). Seismological indicators of geologically inferred fault maturity. *Journal of Geophysical Research: Solid Earth*, *128*(10), e2023JB027096. https://doi.org/10.1029/2023JB027096
Gupta, H. K. (Ed.), (2011). In *Encyclopedia of solid earth geophysics* (Vol. 1). Springer. https://doi.org/10.1007/978-90-481-8702-7
Hamada, Y., Hirono, T., Tanikawa, W., Soh, W., & Song, S.-R. (2009). Energy taken up by co-seismic chemical reactions during a large earthquake: An example from the 1999 Taiwan Chi-Chi earthquake. *Geophysical Research Letters*, *36*(6), L06301. https://doi.org/10.1029/2008GL036772
Henyey, T. L., & Wasserburg, G. J. (1971). Heat flow near major strike-slip faults in California. *Journal of Geophysical Research*, *76*(32), 7924–7946. https://doi.org/10.1029/JB076i032p07924
Hewitt, D. R. (2020). Vigorous convection in porous media. *Proceedings of the Royal Society A: Mathematical, Physical and Engineering Sciences*, *476*(2239), 20200111. https://doi.org/10.1098/rspa.2020.0111
Husseini, M. I. (1977). Energy balance for motion along a fault. *Geophysical Journal of the Royal Astronomical Society*, *49*(3), 699–714. https://doi.org/10.1111/j.1365-246X.1977.tb01313.x
Hutko, A. R., Bahavar, M., Trabant, C., Weekly, R. T., Fossen, M. V., & Ahern, T. (2017). Data products at the IRIS-DMC: Growth and usage. *Seismological Research Letters*, *88*(3), 892–903. https://doi.org/10.1785/0220160190
Ide, S., & Beroza, G. C. (2001). Does apparent stress vary with earthquake size? *Geophysical Research Letters*, *28*(17), 3349–3352. https://doi.org/10.1029/2001GL013106
IRIS DMC. (2013). Data services products: EQEnergy earthquake energy & rupture duration. https://doi.org/10.17611/DP/EQE.1
Jaupart, C., & Mareschal, J.-C. (2003). 3.02—Constraints on crustal heat production from heat flow data. In H. D. Holland & K. K. Turekian (Eds.), *Treatise on geochemistry* (pp. 65–84). Pergamon. https://doi.org/10.1016/B0-08-043751-6/03017-6
Kanamori, H. (1977). The energy release in great earthquakes. *Journal of Geophysical Research*, *82*(20), 2981–2987. https://doi.org/10.1029/JB082i020p02981
Kanamori, H., & Heaton, T. H. (2000). Microscopic and macroscopic physics of earthquakes. In *Geocomplexity and the physics of earthquakes* (pp. 147–163). American Geophysical Union (AGU). https://doi.org/10.1029/GM120p0147
Kanamori, H., Ross, Z. E., & Rivera, L. (2020). Estimation of radiated energy using the KiK-net downhole records—Old method for modern data. *Geophysical Journal International*, *221*(2), 1029–1042. https://doi.org/10.1093/gji/ggaa040
Kano, Y., Mori, J., Fujio, R., Ito, H., Yanagidani, T., Nakao, S., & Ma, K.-F. (2006). Heat signature on the Chelungpu fault associated with the 1999 Chi-Chi, Taiwan earthquake. *Geophysical Research Letters*, *33*(14), L14306. https://doi.org/10.1029/2006GL026733
Karney, C. F. F. (2018). Geographiclib [Software]. Retrieved from https://geographiclib.sourceforge.io/1.49
Lachenbruch, A. H., & Sass, J. H. (1980). Heat flow and energetics of the San Andreas fault zone. *Journal of Geophysical Research*, *85*(B11), 6185–6222. https://doi.org/10.1029/JB085iB11p06185
Lachenbruch, A. H., & Sass, J. H. (1988). The stress heat-flow paradox and thermal results from Cajon Pass. *Geophysical Research Letters*, *15*(9), 981–984. https://doi.org/10.1029/GL015i009p00981
Lachenbruch, A. H., & Sass, J. H. (1992). Heat flow from Cajon Pass, fault strength, and tectonic implications. *Journal of Geophysical Research*, *97*(B4), 4995–5015. https://doi.org/10.1029/91JB01506
Lambert, V., Lapusta, N., & Perry, S. (2021). Propagation of large earthquakes as self-healing pulses or mild cracks. *Nature*, *591*(7849), 252–258. https://doi.org/10.1038/s41586-021-03248-1

Liu, M., Wang, H., & Li, Q. (2010). Inception of the eastern California shear zone and evolution of the Pacific-North American plate boundary: From kinematics to geodynamics. *Journal of Geophysical Research*, *115*(B7), B07401. https://doi.org/10.1029/2009JB007055

Lockner, D. A., & Okubo, P. G. (1983). Measurements of frictional heating in granite. *Journal of Geophysical Research*, *88*(B5), 4313–4320. https://doi.org/10.1029/JB088iB05p04313

Lucazeau, F. (2019). Analysis and mapping of an updated terrestrial heat flow data set. *Geochemistry, Geophysics, Geosystems*, *20*(8), 4001–4024. https://doi.org/10.1029/2019GC008389

McGarr, A. (1976). Seismic moments and volume changes. *Journal of Geophysical Research*, *81*(8), 1487–1494. https://doi.org/10.1029/JB081i008p01487

McGarr, A. (1999). On relating apparent stress to the stress causing earthquake fault slip. *Journal of Geophysical Research*, *104*(B2), 3003–3011. https://doi.org/10.1029/1998JB900083

Milner, K. R. (2014). Third uniform California earthquake rupture forecast (UCERF3) Fault System Solutions [Dataset]. Zenodo. https://doi.org/10.5281/zenodo.5519802

Molnar, P. (1979). Earthquake recurrence intervals and plate tectonics. *Bulletin of the Seismological Society of America*, *69*(1), 115–133. https://doi.org/10.1785/bssa0690010115

Molnar, P., & England, P. (1990). Temperatures, heat flux, and frictional stress near major thrust faults. *Journal of Geophysical Research*, *95*(B4), 4833–4856. https://doi.org/10.1029/JB095iB04p04833

Nielsen, S., Spagnuolo, E., Violay, M., Smith, S., Toro, G., & Bistacchi, A. (2016). G: Fracture energy, friction and dissipation in earthquakes. *Journal of Seismology*, *20*(4), 1187–1205. https://doi.org/10.1007/s10950-016-9560-1

Orowan, E. (1949). Fracture and strength of solids. *Reports on Progress in Physics*, *12*(1), 185–232. https://doi.org/10.1088/0034-4885/12/1/309

Picozzi, M., Bindi, D., Spallarossa, D., Oth, A., Di Giacomo, D., & Zollo, A. (2018). Moment and energy magnitudes: Diversity of views on earthquake shaking potential and earthquake statistics. *Geophysical Journal International*, *216*(2), 1245–1259. https://doi.org/10.1093/gji/ggy488

Pittarello, L., Di Toro, G., Bizzarri, A., Giorgio, P., Hadizadeh, J., & Cocco, M. (2008). Energy partitioning during seismic slip in pseudotachylyte-bearing faults (Gole Larghe Fault, Adamello, Italy). *Earth and Planetary Science Letters*, *269*(1), 131–139. https://doi.org/10.1016/j.epsl.2008.01.052

Popov, A. A., Sobolev, S. V., & Zoback, M. D. (2012). Modeling evolution of the San Andreas Fault system in northern and central California. *Geochemistry, Geophysics, Geosystems*, *13*(8). https://doi.org/10.1029/2012GC004086

Radiguet, M., Cotton, F., Manighetti, I., Campillo, M., & Douglas, J. (2009). Dependency of near-field ground motions on the structural maturity of the ruptured faults. *Bulletin of the Seismological Society of America*, *99*(4), 2572–2581. https://doi.org/10.1785/0120080340

Saffer, D. M., Bekins, B. A., & Hickman, S. (2003). Topographically driven groundwater flow and the San Andreas heat flow paradox revisited. *Journal of Geophysical Research*, *108*(B5). https://doi.org/10.1029/2002JB001849

Scholz, C. H. (2006). The strength of the San Andreas fault: A critical analysis. In *Earthquakes: Radiated energy and the physics of faulting* (pp. 301–311). American Geophysical Union (AGU). https://doi.org/10.1029/170GM30

Shebalin, P., & Narteau, C. (2017). Depth dependent stress revealed by aftershocks. *Nature Communications*, *8*(1), 1317. https://doi.org/10.1038/s41467-017-01446-y

Sibson, R. H. (1973). Interactions between temperature and pore-fluid pressure during earthquake faulting and a mechanism for partial or total stress relief. *Nature; Physical Science*, *243*(126), 66–68. https://doi.org/10.1038/physci243066a0

Takeuchi, C. S., & Fialko, Y. (2012). Dynamic models of interseismic deformation and stress transfer from plate motion to continental transform faults. *Journal of Geophysical Research*, *117*(B5). https://doi.org/10.1029/2011JB009056

The NumPy Contributors. (2023). NumPy: Fundamental package for array computing in Python [Software]. Retrieved from https://pypi.org/project/numpy/

The OpenStreetMap Contributors. (2023). Data derived from openstreetmap for download: Coastlines [Dataset]. Retrieved from https://osmdata.openstreetmap.de/data/coastlines.html

The SciPy Contributors. (2023). SciPy: Fundamental algorithms for scientific computing in Python [Software]. Retrieved from https://pypi.org/project/scipy/

Townend, J., & Zoback, M. D. (2000). How faulting keeps the crust strong. *Geology*, *28*(5), 399–402. https://doi.org/10.1130/0091-7613(2000)28⟨399:HFKTCS⟩2.0.CO;2

USGS, & SCEC. (1991). Southern California Earthquake Data Center. https://doi.org/10.7909/C3WD3xH1

van der Walt, S., Colbert, S. C., & Varoquaux, G. (2011). The NumPy array: A structure for efficient numerical computation. *Computing in Science & Engineering*, *13*(2), 22–30. https://doi.org/10.1109/MCSE.2011.37

Virtanen, P., Gommers, R., Oliphant, T. E., Haberland, M., Reddy, T., Cournapeau, D., et al. (2020). SciPy 1.0: Fundamental algorithms for scientific computing in Python. *Nature Methods*, *17*(3), 261–272. https://doi.org/10.1038/s41592-019-0686-2

Wang, J.-H. (2004). The seismic efficiency of the 1999 Chi-Chi, Taiwan, earthquake. *Geophysical Research Letters*, *31*(10). https://doi.org/10.1029/2004GL019417

Wessel, P., & Smith, W. H. F. (1996). A global, self-consistent, hierarchical, high-resolution shoreline database. *Journal of Geophysical Research*, *101*(B4), 8741–8743. https://doi.org/10.1029/96JB00104

Wessel, P., & Smith, W. H. F. (2017). GSHHG: A global self-consistent, hierachical, high-resolution geography database [Dataset]. Retrieved from https://www.soest.hawaii.edu/pwessel/gshhg/

Yang, T., Chou, Y.-M., Ferré, E. C., Dekkers, M. J., Chen, J., Yeh, E.-C., & Tanikawa, W. (2020). Faulting processes unveiled by magnetic properties of fault rocks. *Reviews of Geophysics*, *58*(4). https://doi.org/10.1029/2019RG000690

Zang, A., Wagner, F. C., Stanchits, S., Janssen, C., & Dresen, G. (2000). Fracture process zone in granite. *Journal of Geophysical Research*, *105*(B10), 23651–23661. https://doi.org/10.1029/2000JB900239

Zeng, Y., Petersen, M., & Boyd, O. (2022). Lower seismogenic depth model for western U.S. earthquakes. *Seismological Research Letters*, *93*(6), 3186–3204. https://doi.org/10.1785/0220220174

Ziebarth, M. J. (2023a). The loaducerf3 Python package [Software]. Retrieved from https://git.gfz-potsdam.de/ziebarth/loaducerf3

Ziebarth, M. J. (2023b). pybalonor: A package for the Bayesian analysis of the log-normal distribution in Python [Software]. Zenodo. https://doi.org/10.5281/zenodo.7896869

Ziebarth, M. J. (2023c). REHEATFUNQ: A Python package for the inference of regional aggregate heat flow distributions and heat flow anomalies [Software]. (V. 1.4.0). https://doi.org/10.5880/GFZ.2.6.2023.002

Ziebarth, M. J., & von Specht, S. (2023). REHEATFUNQ 1.4.0: A model for regional aggregate heat flow distributions and anomaly quantification. *EGUsphere*, 1–57. https://doi.org/10.5194/egusphere-2023-222

Ziebarth, M. J., von Specht, S., Heidbach, O., Cotton, F., & Anderson, J. G. (2020). Applying conservation of energy to estimate earthquake frequencies from strain rates and stresses. *Journal of Geophysical Research: Solid Earth*, *125*(8), e2020JB020186. https://doi.org/10.1029/2020JB020186

References From the Supporting Information

Convers, J. A., & Newman, A. V. (2011). Global evaluation of large earthquake energy from 1997 through mid-2010. *Journal of Geophysical Research*, *116*(B8), B08304. https://doi.org/10.1029/2010JB007928

Fabrizi, E., & Trivisano, C. (2012). Bayesian estimation of log-normal means with finite quadratic expected loss. *Bayesian Analysis*, *7*(4), 975–996. https://doi.org/10.1214/12-BA733

Gardini, A., Trivisano, C., & Fabrizi, E. (2020). Bayesian inference for quantiles of the log-normal distribution. *Biometrical Journal*, *62*(8), 1997–2012. https://doi.org/10.1002/bimj.201900386

Gradshteyn, I. S., & Ryzhik, I. M. (2007). In A. Jeffrey & D. Zwillinger (Eds.), *Table of integrals, series, and products* (7th ed.). Academic Press.

Kanamori, H., & Anderson, D. L. (1975). Theoretical basis of some empirical relations in seismology. *Bulletin of the Seismological Society of America*, *65*(5), 1073–1095. https://doi.org/10.1785/BSSA0650051073

Olver, F. W. J., Olde Daalhuis, A. B., Lozier, D. W., Schneider, B. I., Boisvert, R. F., Clark, C. W., et al. (2020). NIST digital library of mathematical functions. Retrieved from http://dlmf.nist.gov/

Sibson, R. H. (1974). Frictional constraints on thrust, wrench and normal faults. *Nature*, *249*(5457), 542–544. https://doi.org/10.1038/249542a0

Yamaji, A. (2007). *An introduction to tectonophysics: Theoretical aspects of structural geology*. Terrapub Tokyo.